Single Cell Multi-Omics of an iPSC Model of Human Sinoatrial Node Development Reveals Genetic Determinants of Heart Rate and Arrhythmia Susceptibility

James L. Engel[1,2,3,*], Xianglong Zhang[4,*], Daniel R. Lu[5], Olaia Fernandez Vila[5], Vanessa Arias[5], Jasper Lee[5], Christopher Hale[5], Yi-Hsiang Hsu[4], Chi-Ming Li[5], Vasanth Vedantham[2,3,6,#], Yen-Sin Ang[1,#]

[1]Cardiometabolic Disorders, Amgen, Inc., South San Francisco, CA; [2]Cardiology Division, Department of Medicine; [3]Cardiovascular Research Institute University of California, San Francisco, CA; [4]Center for Research Acceleration by Digital Innovation, Amgen, Inc., South San Francisco, CA and Cambridge, MA; [5]Research Biomics, Amgen Inc., South San Francisco, CA and [6]Cardiovascular Genetics Center, University of California, San Francisco, CA

*These authors contributed equally

#Co-corresponding authors

Corresponding Authors:

Yen-Sin Ang, PhD
Amgen, Inc.
750 Gateway Blvd Suite 100
South San Francisco, CA 94080
yang02@amgen.com

Vasanth Vedantham, MD, PhD
Smith Cardiovascular Research Building
555 Mission Bay Blvd South, 352M
San Francisco, CA 94158
TEL: 415-476-7559
FAX: 415-476-6260
vasanth.vedantham@ucsf.edu

ABSTRACT

Defining the molecular and genetic basis for heart rate regulation and for susceptibility to atrial arrhythmias has been challenging due to the complexity of the human sinoatrial node (SAN), a tiny structure with limiting numbers of several distinct pacemaker cardiomyocyte (PC) subtypes in a spatially patterned array. Here we describe a novel method to derive large numbers of human PCs from human induced pluripotent stem cells (hiPSCs) that recapitulates key features of SAN development including differentiation into anatomically and functionally distinct PC subtypes of the SAN. Single cell (sc) RNA-sequencing, sc-ATAC-sequencing, and time course analyses of cellular differentiation were used to define epigenetic and transcriptomic signatures of cellular specialization within the SAN, and to identify transcriptional pathways important for PC differentiation. Intersection of our multi-omics datasets with existing human genome wide association studies uncovered regulatory elements with differential accessibility in different PC subtypes that harbored SNPs that associated with human heart rate regulation and susceptibility to atrial fibrillation, enabling disease gene discovery and prioritization.

INTRODUCTION

Heart rhythm originates in the sinoatrial node (SAN), an array of several thousand specialized pacemaker cardiomyocytes (PCs) and non-myocyte cells located at the junction of the systemic venous inflow with the right atrium[1]. The SAN possesses a complex spatial organization that includes a head region that wraps anteriorly around the superior vena cava, a tail region that extends into the inter-caval groove, and a transition zone at the interface of the SAN and atrial myocardium, with distinct PC subtypes occupying each region[2,3]. Head PCs, Tail PCs, and Transition Zone PCs have distinct phenotypes and gene expression programs that allow for optimal SAN impulse generation, impulse transmission to the atrium, and autonomic response[4,5]. Characterizing the differentiation programs of each human PC subtype has been challenging due to the low cell numbers and inaccessibility of human SAN tissue, creating an obstacle to developing a detailed genetic and pathophysiological understanding of SAN dysfunction and atrial arrhythmias, among the most common and morbid heart rhythm disorders.

Human induced pluripotent stem cells (hiPSCs) can be differentiated into various cardiomyocyte subtypes, including atrial[6], ventricular[7], and pacemaker[8-10]. Recent work has shown that PC subtypes can be discerned from hiPSC-based differentiations using single cell (sc)-RNA sequencing and clustering analysis[11], raising the possibility of using *in vitro* systems to dissect the development of the SAN, including identification and perturbation of the molecular determinants of key steps in lineage commitment. Developing such a program will require a robust, scalable differentiation protocol that can be used to generate large-scale expression and epigenetic datasets at the single cell level. Equally important, integration of such datasets with human genetic data and clinical phenotypes will be essential to leverage the power of *in vitro* differentiation systems to yield insights into normal human function and disease.

Here, we describe a novel and scalable monolayer hiPSC SAN differentiation protocol that yields large numbers of SAN head, SAN tail, and transition zone PCs, as well as sinus venosus cardiomyocytes and non-myocyte cells. scRNA-seq and sc-ATAC-seq was performed on over 100,000 cells from these differentiations, allowing for detailed characterization of PC subtypes and trajectory analysis, providing new insights into the

epigenetic and transcriptional determinants of PC subtype identity. Integration of multi-omics datasets with existing genome wide association studies allowed us to establish specific associations of discrete cell types with clinical phenotypes. Moreover, by limiting genomic analysis to regions with open chromatin, our datasets allowed us to improve the power of existing genome wide association studies and we identified several novel genes associated with arrhythmia susceptibility. Taken together, our SAN differentiation protocol and single cell datasets provide a new resource that will allow for molecular dissection of the determinants of human heart rhythm and arrhythmias.

RESULTS

Differentiation of Sinoatrial Node-Like Cardiomyocytes for Multi-Omics Profiling.

To develop a protocol to differentiate Sinoatrial Node-Like Cardiomyocytes (SANCMs), we modified established monolayer differentiation protocols for ventricular cardiomyocytes (VCM) and atrial cardiomyocytes (ACMs) [12-14] by incorporating key aspects of an embryoid body-based SANCM derivation protocol [8] (Fig.1a). Specifically, we supplemented the ACM differentiation with BMP4 and the TGFβ inhibitor SB431542 at 72 hours post mesoderm induction, with subsequent addition of the FGF inhibitor PD173074 for 48 hours beginning at 96 hours post induction. All cardiomyocyte differentiations were carried out for 20 days before passaging and metabolic selection for 8 days to enrich for CMs [15]. As expected, beating rate as determined by multielectrode array recordings for the three CM subtype differentiations beginning at day 9 showed large differences in firing frequency, with SANCMs eventually beating at 2.8 +/- 0.1 Hz, ACMs 2.1 +/- 0.1 Hz, and VCM 1.3 +/- 0.1 Hz (n = 4 wells for each condition, Extended Data Fig. 1a).

We next performed qPCR on the three independent batches of differentiations to measure relative expression levels of cardiomyocyte subtype-specific markers. While cells from all three differentiation protocols expressed the cardiomyocyte markers *TNNT2*, *NKX2-5*, *ACTN2*, *MYH6, and SCN5A* (Fig.1b and Extended Data Fig. 1b), expression levels of chamber-specific markers differed among VCMs, ACMs, and SANCMs. VCM cells were enriched for ventricular chamber markers *MYL2*, *IRX4, MYH7* and *HEY2* (Fig.

1c and Extended Data Fig. 1c), while ACMs were enriched for *NPPA*, *MYL7*, *NR2F2* and *KCNA5* (Fig. 1d and Extended Data Fig. 1d).

Compared to VCMs, SANCMs were enriched for pacemaker lineage-determining transcription factors *TBX18*, *SHOX2*, and *ISL1* (Fig. 1e), and ion channels *HCN1*, *HCN4*, *KCNJ3* (Fig. 1f). Of note, *NKX2-5*, a transcription factor that is downregulated in the SAN, also showed a non-significant reduction in the SANCM cultures. When compared to the ACMs differentiation, SANCMs were significantly enriched for both *TBX18* and *SHOX2* but not for the other SAN marker genes, possibly reflecting the presence of significant numbers of pacemaker-like cells in the ACM differentiation, as has been previously described [6,16]

To define relative protein expression levels of selected genes at the level of individual cells, we performed quantitative immunocytochemistry for *TNNT2*, *NKX2-5*, *SHOX2*, *ISL1*, and *HCN4* in randomly selected high-power fields from 2 replicates each of VCM and SANCM differentiations (Fig. 1g and Extended Data Fig 1e). More than 95% of cells visualized in both differentiations were *TNNT2*+, as expected (Extended Fig 1f). For SANCMs, 65% were SHOX2+, 75% were ISL1+ and 79% were HCN4+ as compared to 4%, 8% and 23% of VCMs, respectively ($p < 0.0001$ for each gene; Fig. 1h and Extended Data Fig 1e,f). For NKX2-5, 34% of SANCMs were positive while 85% of VCMs were positive and the average signal intensity per positive nucleus was reduced by 50% in SANCMs, a degree of downregulation that comports well with findings from RNA sequencing datasets of SAN from animal models (Fig. 1h and Extended Data Fig 1f).

Action potential waveforms from spontaneously beating VCM and SANCM cells were recorded using a voltage-sensitive dye (n = 399 for VCMs and n = 169 for SANCMs). We observed expected differences in AP morphology – VCMs exhibited a steeper phase 0 and prolonged phase 2, while SANCMs exhibited more rapid diastolic depolarization and shorter cycle length (Fig. 1i). Measurement of APD20, APD50, and APD90 revealed a shorter APD in SANCMs, and determination of action potential amplitude using arbitrary units showed that SANCMs have a smaller AP amplitude (Fig. 1i and Extended Data Fig. 1g). SANCMs were also sensitive to application of Zatebradine, a specific blocker of HCN channels, indicating a higher density of HCN channels in the SANCMs (Fig. 1j). Taken

together, these results demonstrate that our scalable SANCM differentiation protocol yields large numbers of pacemaker-like cardiomyocytes suitable for multi-omics profiling.

Single-Cell Transcriptomics Reveals Distinct Human Atrial, Ventricular, and SAN Populations *In Vitro*.

Next, we performed single cell RNA sequencing (scRNA-seq) on day 34 VCMs, ACMs, and SANCMs from 3 independent differentiations per cardiomyocyte subtype (n = 21,000 – 22,000 cells total per differentiation condition, Extended Data Fig. 2a). Unsupervised clustering and dimension reduction was carried out for all cells and plotted in the same UMAP space. Cells derived from VCM, ACM, and SANCM directed differentiations occupied distinct regions in the UMAP space with minimal overlap, indicating unique molecular signatures (Fig. 2a). We identified a total of 26 clusters, with the largest number of cells representing cardiomyocytes as demonstrated by expression of pan-cardiac markers *TNNT2, ACTN2,* and *MYH6* (Fig. 2b,c). Using a cell composition cut-off of 70%, 8, 3 and 6 clusters originated from the ACM, SANCM, and VCM differentiation, respectively, with the remaining clusters representing cells derived from multiple differentiations (Extended Data Fig. 2b).

Individual clusters were assigned to cardiomyocyte subtypes using their marker genes as well as established expression patterns (Fig. 2d,e and Extended Data Fig. 2c). Supporting our qPCR results, clusters 2, 7, 9, 15 represent VCMs (*MYL2, MYH7, HEY2, IRX4,* and *HOPX*), clusters 0, 6, 8 and 12 represent ACMs (*MYL7, NPPA, NR2F2. KCNJ3,* and *KCNA5*) and cluster represent PCs (*SHOX2, ISL1, TBX18,* and *TBX3*). We also identified several clusters that did not express the pan-myocardial markers *TNNT2*, *ACTN2*, and *MYH6* (C10, C13, C14, C17, C19, C20, C21, C23, C24 and C25). From these non-cardiomyocyte clusters, we identified small fractions of proepicardial cells (C25) marked by *WT1, ALDH1A2, BNC1,* and *PDPN*, endocardial cells (C13, C19) marked by *FOXC1, MSX1, NRG1, NPR3* and *NFATC1*, primitive mesendoderm marked by *FOXA2, EOMES, MESP1* and *MESP2* (C17, C21), and visceral neurons marked by *PHOX2B, PRPH,* and *CHRNA3* (C24) (Fig. 2b,c and Extended Data Fig. 2d-h)

Differential expression analysis between SANCMs and ACMs yielded 506 genes that recapitulated well-established differences between atrial and PCs[17] (Fig. 2f). GO

analysis of these DEGs demonstrated enrichment of biological processes related to sinoatrial node development, cardiac conduction, and regulation of heart contraction (Fig. 2g). Detailed comparison of the list of DEGs with previously published neonatal mouse[18] and human fetal[19] SAN versus right atrium comparative transcriptomic datasets demonstrated significant overlap among the three datasets (Extended Data Fig. 2i p = 0.02 for overlap between SANCMs and human dataset and $p = 6.4 \times 10^{-7}$ for overlap between SANCMs and mouse dataset), underscoring the fidelity of the hiPSC-SANCM differentiation.

Sub-clustering of SAN Differentiation Identifies Specialized PC Subtypes.

The functional organization of the SAN, diagrammed in Fig. 3a, includes an autonomically responsive SAN head located cranially, an SAN tail extending inferiorly along the venous valves, and a transition zone that facilitates source-sink matching between SAN and atrium[3]. Different pacemaker subtypes express different levels of key transcriptional regulators that guide their distinctive phenotypes[20] (Fig. 3b).

To test whether our SAN differentiation yielded any or all of these PC subtypes, we performed a sub-clustering analysis on SANCMs that yielded 11 clusters, each of which could be assigned to a venous pole population (Fig. 3c). Using differential expression of SAN and myocardial transcription factors, we associated cluster 2 with SAN head cells (*TBX18*^{HI}/SHOX2^{+}/ISL1^{HI}/*TBX3*$^{+}$/*NKX2-5*^{LOW}), clusters 0 and 3 with SAN tail cells (TBX18^{-}/SHOX2^{+}/ISL1^{LOW}/TBX3^{+}/NKX2-5^{+}), clusters 1 and 4 with transitional cells (*TBX18*$^{-}$/SHOX2^{+}/ISL1^{-}/*TBX3*^{LOW}/*NKX2-5*^{HI}), and clusters 6, 7, and 8 with sinus venosus myocardium (*TBX18*$^{+}$/SHOX2^{+}/ISL1^{LOW}/*TBX3*$^{-}$/*NKX2-5*^{LOW}). The two SAN tail cell clusters were distinguished by differential expression of the SAN transcriptional repressor *TBX3* and its downstream target genes such as *NPPA*, possibly reflecting residual heterogeneity within these populations or varying degrees of maturation within the SAN tail cells at D34. (Fig. 3c). Notably, cluster 5 most resembled sinus venosus myocardium but was lower in *TBX18* expression than other sinus venosus clusters. We annotated 2 small populations of non-myocyte cells as proepicardial (cluster 9) and visceral neurons (cluster 10) based on their cluster-defining genes (Fig. 3d).

Closer examination of the two major PC subtypes (SAN head and SAN tail cells) identified several hundred DEGs between SAN head (C2) and SAN tail (C0+C3) populations, encompassing GO terms for numerous biological processes related to cellular morphogenesis, cytoskeletal organization, cell adhesion, and neuron protrusion/axon development (Fig. 3e and Extended Data Table 1). Further subclustering of only SAN Head and SAN Tail cells demonstrated contrasting expression of *TBX18* and *NKX2-5* with uniformly high-level expression of *SHOX2* throughout and a gradient of *ISL1* expression from SAN head ($ISL1^{HI}$) to SAN tail ($ISL1^{LOW}$) cells (Fig. 3f,g).

To test whether these differences recapitulated what has been observed *in vivo*, we intersected our list of DEGs with a list of DEGs derived from mouse neonatal SAN head and SAN tail cells. 15 out of 85 mouse SAN head vs tail DEGs were also differentially expressed between C2 (SAN head-like) and C0+C3 (SAN tail-like), an odds ratio of 7.8 over SAN-expressed genes that were not on the mouse head versus tail DEG list ($p = 2.6 \times 10^{-8}$ by Fisher's exact test, Fig. 3h). The list of shared DEGs between mouse and human included canonical transcription factors *ISL1, TBX18, SHOX2* and *NKX2-5*, supporting the existence of an evolutionarily conserved blueprint not only for SAN development broadly but also for fine patterning of PC subtypes within the entire node. Other SAN Head vs Tail DEGs that were conserved between mouse and human included *GJA1*, an established downstream target of *NKX2-5* (enriched in SAN tail), modulators of signal transduction (*FHL2*, *VSNL1*, *BMP2*), and cytoskeletal organizing proteins (*MARCKS, TMSB4X*). In addition, we also observed conserved enrichment in SAN head of *NF1A*, a transcription factor without a previously known role in SAN development.

Finally, to test whether our cluster assignments agreed with SANCM differentiations using other methodologies, we projected scRNA-seq data from a recently published hiPSC SAN differentiation into our UMAP and found very close agreement in cluster assignments between the two protocols, such that 94% of SAN head cells mapped to either our SAN head cluster (C2) or to the narrow interface between our SAN head and the nearest SAN tail clusters (C2/C3 interface); 90% of SAN tail cells mapped to our SAN tail clusters (C0+C3); 82% of transitional cells mapped to our transitional clusters (C1+C4), 64% of sinus venosus cells mapped to our sinus venosus clusters (C5+C6+C7+C8), and 97% of proepicardial cells mapped our proepicardial cluster (C9)

(Extended Data Fig 3a). Overall, the concordance of our SAN head versus tail differential expression analysis with findings from primary mouse SAN cells and with previous hiPSC-based SAN differentiation protocols strongly supports our conclusion that the SANCM differentiation yields specialized venous pole cardiomyocytes that faithfully reflect distinct PC subtypes.

scATAC-seq Identifies Enhancers in SANCM Subtypes

The distinct transcriptomes of specialized PC subtypes prompted us to test whether distinct epigenetic signatures could also be assigned to our SANCMs by performing single cell assay for transposase accessible chromatin with sequencing (scATAC-seq). UMAP projection identified 8 clusters (Fig. 4a and Extended Data Fig. 4a) which we annotated based on predicted expression of canonical SANCM marker genes: *ISL1*$^{+}$/*TBX18*$^{+}$/*SHOX2*$^{+}$/*NKX2.5*^{LOW} SAN head (C2), *ISL1*$^{+}$/*SHOX2*$^{+}$/*NKX2.5*$^{+}$/*TBX18*^{LOW} SAN tail (C1, C4, C6), *NKX2.5*^{HIGH}/*SHOX2*^{LOW}/*TBX18*$^{-}$ transitional cells (C0, C5), and TBX18+/NKX2-5- sinus venosus cells (C3) (Fig. 4b). Gene expression profiles for each cluster were based on chromatin accessibility using Peak2gene correlations (Figure 4C, left), then matched with gene expression levels measured in the corresponding cell cluster (Figure 4C, right). This analysis demonstrated concordance between the transcriptional and epigenetic status of each cell subtype.

The strong chromatin-mRNA correlation permitted us to establish distal enhancer-promoter links of up to several hundred kilobases, along with quantitative estimation of interaction strengths. Genomic tracks for accessibility, marker peaks and Peak2gene links in different SANCM subtypes are shown for *SHOX2*, *ISL1*, *TBX3*, and *TBX18* (Fig. 4d-f and Extended Data Fig. 4b). Regions of differential accessibility between SAN subpopulations were observed at cis-regulatory elements that were reported to activate these genes (Fig. 4d-f and Extended Data Table 2) and numerous cluster-enriched ATAC-seq peaks were identified (Extended Data Fig. 4c). For example, the syntenic region to a mouse Isl1 enhancer previously characterized by our group in detail demonstrated differential accessibility in PCs (SAN head and tail) as compared to more atrial-like transitional cells (Fig. 4d), analogous to ISL1 mRNA levels in these subpopulations. In addition, our analysis identified other ISL1 enhancers linked to

transcription that have been previously validated in a zebrafish system. Examination of the *SHOX2* and *TBX3* loci demonstrated linkage of previously defined SAN enhancers to transcription and simultaneously showed differential accessibility across the different venous pole cardiomyocyte subtypes. Remarkably, the only peak-to-gene links over a 1-Mb window near *TBX3* identified an enhancer known to be functionally important in PCs. Comparison with a published dataset on a mixed SANCM population revealed that most of the ATAC-seq signal were derived from SAN head cells, with some contribution from SAN tail cells, suggesting that the upstream processes that regulate accessibility of the *TBX3* enhancer are critical for fine-patterning of the SAN (Fig. 4f). Finally, reclustering of the SAN head and SAN tail cells alone demonstrated expected patterns of predicted gene expression for canonical SAN transcriptional regulators, similar to what was observed for transcriptomic datasets (Extended Data Fig. 4d).

Identification of Transcriptional Pathways Important for SAN Subtype Differentiation.

To identify transcriptional pathways that drive cellular subtype-specific differentiation programs, we performed motif enrichment analysis on each cluster (Fig. 4g and Extended Data Table 3). This analysis resulted in association of canonical myocardial transcription factors MEF2, TBX5, and NKX2-5 with the more atrial-like transitional cells, whereas marker peaks for the main SAN Tail cluster (C1) demonstrated enrichment of ISL and GATA binding sites, as well as sites for the TALE-class transcription factors MEIS and TGIF. The SAN Head cluster (C2) exhibited the strongest enrichment for the NFI sites, followed by ISL1, while the sinus venosus cluster (C3) demonstrated strong enrichment for AP-1 sites. These findings are underscored by a direct comparison of motif enrichment between SAN Head and SAN Tail marker peaks, in which NFI sites were strongly enriched in SAN head whereas motifs for myogenic factors NKX2-5 and MEF2 where strongly enriched in SAN tail (Fig. 4h and Extended Data Table 4). Motif enrichment analysis for the subset of ATAC-seq peaks that were positively linked to transcription via Peak2Gene analysis identified the top 20 positive transcriptional regulators across the dataset (Fig. 4i). This analysis identified known regulators of SAN development ISL1, TBX5, and MEF2 but also identified NFI motifs, which exhibit cellular subtype-specific

motif enrichment and differential gene expression (NFIA) in SAN head versus other venous pole cardiomyocytes. These data support a model in which distinct transcriptional circuitry – some not previously characterized in the SAN – drive sub-specialization of venous pole cardiomyocytes and control functional patterning of the node.

Time Course scRNA-seq Anaysis of hiPSC-Derived SANCM Recapitulates *In vivo* Developmental Transitions

To explore the origin of the distinct transcriptional programs of venous pole cardiomyocyte subtypes, we performed scRNA-seq on cells from D3, D4, D6, D10, and D23 of SANCM differentiation (Extended Data Fig. 5a). Unsupervised clustering and dimension reduction was carried out on data from all the cells, resulting in the identification of a total of 37 clusters. Individual clusters were annotated and classified based on their gene expression profiles and generally clustered together in UMAP space by differentiation timepoint (Fig. 5a and Extended Data Table 5).

To define cellular intermediates along the differentiation pathway from hiPSCs into the different SAN cell types, we performed pseudotime trajectory analysis using the partition-based graph abstraction (PAGA) method, resulting in a similarity-based connectivity map (Extended Data Fig. 5b) that generated a model for the cellular lineage tree (Fig. 5b). The central SANCM differentiation pathway identified by our analysis contained 11 different cell types throughout differentiation from D3 to D34. The earliest branch point occurred at day 3 when a subset of cardiac progenitors (C6) differentiated down a mesenchymal/fibroblast pathway and a separate population of endoderm progenitors arose (C16).

The next major branch point along the main differentiation pathway occurred between D6 and D10, when TBX18^{+} progenitors (cluster 14) split into three branches corresponding to epicardial, pacemaker, and sinus venosus lineages. By D34, each of the PC subtypes (SAN head, SAN tail, and transitional cells) were resolvable as separate clusters in the UMAP. To visualize differentiation towards PCs, we plotted each cluster along the main differentiation pathway using diffusion pseudotime analysis (Fig. 5c). These plots demonstrate that much of the movement towards fully differentiated pacemaker phenotypes occurred between D10 and D23. In addition, between D23 and

D34, when PC subtypes are resolved as separate clusters, PC progenitors (C28) and the differentiated PC subtypes (C0, C2, and C26) are relatively close in pseudotime. Indeed, C0, C2, and C26 appear to emerge simultaneously in the hiPSC system from a common pool of progenitors (C28) rather than differentiating sequentially, raising the possibility that PC subtypes are specified earlier in the differentiation pathway than D23 (Fig. 5d).

To test this possibility, we subclustered key populations along the SAN differentiation pathway, including C14 (*TBX18*$^{+}$ progenitors) and C28/C5 (SAN progenitors). This analysis revealed heterogeneity in expression of key venous pole myocardial transcription factors *TBX18*, *SHOX2*, *NKX2-5*, and *ISL1* at each of these key timepoints. Subclustering of C14, appearing at D6, already exhibited a discrete *TBX18*$^{+}$/*SHOX2*$^{+}$/*ISL1*$^{+}$ myocardial population that occupied a separate region of the UMAP compared to other TBX18 progenitors, suggesting that specification of pacemaker myocardium occurred between D3 and D6 of the differentiation (Fig. 5e). Subclustering of C5, appearing at D10, revealed populations that resembled SAN head (*TBX18*$^{+}$/*ISL1*^{HIGH}/*SHOX2*^{HIGH}/*NKX2-5*$^{-}$), SAN tail (*TBX18*$^{-}$/*ISL1*^{LOW}/*SHOX2*^{HIGH}/*NKX2-5*^{LOW}) and transitional/atrial (*TBX18*$^{-}$/*NKX2.5*$^{+}$), suggesting that PC subtypes may also adopt their fates relatively early with progressive differentiation into discretely resolvable clusters by D34 (Fig. 5f). Importantly, this analysis suggests that some *TBX18*$^{+}$ myocardial progenitors downregulate *TBX18* expression during differentiation towards SAN tail or transitional phenotypes, as has been observed *in vivo* during murine cardiogenesis.

To define the molecular correlates of SANCM differentiation in the hiPSC system, we examined the two key nodes in the main differentiation pathway using differential expression analysis between progenitor populations and their putative progeny. Pairwise comparison of D6 TBX18+ progenitors with epicardial, sinus venosus myocardium, and pacemaker myocardium revealed that the majority of pacemaker progenitors upregulated expression of pan-myocardial genes including *ACTC1*, *MYH6*, *RYR2*, *TTN*, *SLC8A1*, and *NKX2-5* (Fig. 5g). However, although increased compared to the progenitor state, only a small percentage of pacemaker progenitors expressed *NPPA*, consistent with its general exclusion from the differentiated SAN. The finding that most pacemaker progenitors expressed *NKX2-5* supports a recent finding in zebrafish of transient upregulation

followed by repression of an *NKX2-5*-dependent myogenic program after pacemaker specification but prior to differentiation. By contrast, progenitors of the sinus venosus myocardium upregulated a hybrid smooth muscle/myocardial gene program that included *FN1*, *COL3AL1* as well as *SHOX2* and *PLN* (Extended Data Fig. 5c).

Comparison of D23 SAN progenitors with D34 pacemaker subtypes revealed downregulation of *SHOX2* in more atrial-like transitional cells and upregulation of *SHOX2* in both SAN head and SAN tail, while only the SAN head upregulated *TBX18* and downregulated *NKX2-5*. In addition, both *BMP4* expression and *WNT2* expression were downregulated in the transitional cells (Fig. 5h). Gene ontology analysis of upregulated genes in each of the SAN cardiomyocyte subtypes revealed several common biological processes related to cardiac and SAN development with each subtype enriched for genes associated with some unique GO terms (Extended Data Table 6)

Integration of Multi-Omics Data with Human Genetic Data for Gene Discovery and Annotation

To test whether accessible chromatin regions in different SANCM subtypes occurred in regions that were linked to single nucleotide polymorphisms relevant to heart rhythm-related traits, we first generated Manhattan plots restricted to genomic regions within 0.5 kb of accessible chromatin regions in our scATAC-seq datasets using summary statistics from previously published GWAS for resting heart rate and for atrial fibrillation (Fig. 6 and Extended Data Fig. 6a,b). SNPs in linkage disequilibrium were filtered to narrow the number of SNPs tested. This analysis recapitulated most of the known genetic associations identified in the source studies (Extended Data Fig. 6c,d and Extended Data Table 7), underscoring the relevance of non-coding regulatory regions to heritable genetic variation.

We hypothesized that accessible chromatin regions that mark different SANCM cell types might exhibit cell type-specific association strengths and effect sizes for heart rhythm-related traits. To test this possibility, we overlapped summary statistics from GWASs for many cardiac and non-cardiac traits with ATAC-seq marker peaks for each cluster from our scATAC-seq dataset and calculated the enrichment of significant SNPs near accessible chromatin regions for each trait and scATAC-seq cluster (Fig. 6a). As

expected, traits that are not directly related to cardiac physiology did not show any significant associations with accessible chromatin regions in SAN cardiomyocyte cell types while many cardiac structural and functional traits did show differing degrees of association. Resting heart rate was significantly associated with marker peaks only for SAN tail and transitional cells but not for SAN head, while heart rate recovery after exercise (an indicator of cardiac autonomic responsiveness) was only significantly associated with SAN head peaks, supporting current models for functional compartmentalization of the SAN.

Remarkably, the strongest association based on significance and false discovery rate across all clusters was for atrial fibrillation, a heart rhythm disorder that is closely associated with sinus node function. We wondered whether an integrative genomic analysis could provide insight into this poorly understood association, and whether we could use our dataset to facilitate novel gene discovery. Because we only considered SNPs that overlapped with regions of DA chromatin, and we pruned SNPs in LD with one another, fewer SNPs were tested overall allowing for a higher P value significance cut-off that is generally used for genome-wide significance (5×10^{-8}), resulting in our identification of 24 new AF-associated loci that overlap with accessible chromatin in SANCMs (Fig. 6b-d), including *ALDH8A1*, a component of the retinoic acid biosynthetic pathway, cardiac transcription factor *TBX20*, and presumed zinc finger transcription factors with no known cardiac function thus far including *ZFAND3* and *ZFYVE1*.

DISCUSSION

In this work we used single cell multi-omics on hiPSCs-derived PCs to demonstrate that key aspects of *in-vivo* SAN development and function can be modelled *in vitro*, including differentiation of distinct PC subtypes and identification of genomic loci that influence heritability of heart rhythm phenotypes and propensity to arrhythmias.

Large Scale Differentiation of PCs for Genomic and Functional Analysis

Because PCs comprise a tiny fraction of cardiomyocytes, the potential of a stem cell-based derivation protocol to yield enough material for genomic analyses has long

been appreciated. Over the past decade, several protocols have been developed to generate SAN cells from cardiomyocytes, including selection for cells expressing pacemaker markers from mixed populations of hiPSC-derived cardiomyocytes[21], directed differentiation using exposure to morphogens and growth factors[8,22], overexpression of transcription factors[23-25], and directed differentiation using small molecules.

We used a refinement of a growth factor-based approach that recapitulates key signals that are present during embryonic development, first described by Protze et al. (2017). Biphasic Wnt signaling promotes cardiomyogenesis, after which retinoic acid introduces a posteriorizing signal that represses ventricular gene expression and promotes atrial gene expression. SANCM differentiation is further driven by inhibition of TGFβ and FGF signaling. Our results compare favorably with other approaches, as evidenced by gene expression, chromatin accessibility, and electrophysiological behavior of SANCMs. The ability to generate these cells in monolayer and at scale opens a path to carrying out genomic analyses including chromatin immunoprecipitation for PC-enriched transcription factors, chromatin conformation capture, and to employ screening using CRISPR or small molecules with physiological or imaging-based readouts, substantially expanding the ability to interrogate the biology of cardiac automaticity.

Single cell genomic analysis allowed for assessment of the purity of differentiation into our targeted cell types and for higher resolution comparison of iPSC-derived cells with their *in-vivo* counterparts. Notably, the minimal overlap of VCMs, ACMs, and SANCMs in the D34 scRNA-seq clustering demonstrates that the SANCM differentiation generates cardiomyocyte subtypes that are not observed in significant quantities in the VCM differentiation or ACM differentiations. Therefore, attempting to select for PCs from non-directed differentiation protocols is likely to yield small percentages of the desired cell populations and would support a directed differentiation approach over a selection-based approach.

Derivation of Functionally Specialized PC Subtypes

Based on anatomical location, functional compartmentalization, and gene expression patterns, the right venous pole contains distinct subsets of specialized myocardium including sinus venosus myocardium, SAN head myocardium, SAN tail

myocardium, and transitional myocardium. Each subtype is distinguishable by differential expression of transcription factors including TBX18, ISL1, SHOX2, TBX3, and NKX2-5, and each SAN cell type is specialized to perform a different role in cardiac impulse generation and transmission.

Subclustering of our SANCMs recapitulated these anatomical and functional divisions and allowed us to define sets of differentially expressed genes that mark each PC subtype. These DEGs significantly overlapped with an scRNA-seq dataset derived from mouse neonatal SAN[26], indicating that not only is the basic blueprint of the SAN deeply conserved, but fine-patterning of the SAN into a head and tail region involves conserved gene regulatory networks. Further exploration of these gene sets will likely provide insight into how functional properties of different PC subtypes are regulated at the molecular level. Merging of our data with a recent scRNA-seq dataset for hiPSC-derived SANCMs using a somewhat different protocol and sequencing methodology resulted in close agreement in cluster assignments, supporting the notion that PCs diversify *in vitro* during SAN differentiation across multiple platforms[11]. In theory, the ability to derive relevant PC subtypes could permit realistic modelling of cardiac automaticity using a tissue engineering approach, historically a daunting task given the complexities of SAN microanatomy and the physiology of source-sink current matching at the SAN-atrium interface.

Novel Transcriptional Pathways Implication in PC Development

The identification of PC subtypes was further supported by our scATAC-seq analysis, which closely correlated with the scRNA-seq analysis. Aggregating scATAC-seq data by cluster demonstrated differentially accessible chromatin regions associated with different PC subtypes and included enhancers that have been previously defined for SAN transcription factors SHOX2, ISL1, TBX3, and novel enhancers for TBX18. By demonstrating DA chromatin at these enhancers between SAN head, SAN tail, and transitional cells, our data suggest that the signaling upstream of these established SAN enhancers is involved not just in specification but also in fine patterning of the SAN. In addition, motif enrichment analysis demonstrated two novel transcriptional pathways. First, AP-1 motifs are highly overrepresented in peaks from sinus venosus myocardium,

suggesting that this pathway could be critical for differentiation of this cell types from SAN myocardium. Of note, sinus venosus myocardium exhibited a hybrid cardiomyocyte-smooth muscle gene program, so one possibility is that AP-1 may promote formation of TBX18+ progenitors and that persistent AP-1 activity could direct TBX18+ progenitors towards a sinus venosus fate. Future work directed at perturbing AP-1 in our culture system could test whether blocking or promoting AP-1 activity could bias the differentiation away from or towards sinus venosus myocardium. ATAC-seq data from mouse SAN revealed that AP-1 motifs are highly overrepresented in differentially accessible chromatin in neonatal mouse PCs as compared to atrial myocardium, suggesting an evolutionarily conserved role for AP-1 in regulating SAN gene expression[18].

In addition, we found that the NFI motif was highly overrepresented specifically in SAN head myocardium as compared to SAN tail myocardium and that *NFIA* and *NFIB* expression was enriched in SAN head cells. Further supporting a role for this novel pathway in SAN subtype differentiation, comparison of our scRNA-seq with a mouse dataset demonstrated that *NFIA* is differentially expressed in mouse SAN head versus SAN tail cells[26]. Although a recent study has shown that loss of NFIX transcription factor in mice results in altered adult SAN physiology without other effects on cardiac structure and function[27], NFI transcription factors have not been previously explored in the context of SAN development. Our *in vitro* system will permit further work on NFI-dependent mechanisms involved in SAN patterning. Finally, integrative analysis of scRNA-seq and scATAC-seq demonstrated that selected motifs were associated with activating transcription in SANCMs, including ISL1, TBX, MEF2, and NFI. Notably, despite the importance of NKX2-5 in SAN differentiation, it did not emerge as a positive transcriptional regulator in the SAN dataset, consistent with its hypothesized role as a repressor of pacemaker gene expression and a positive regulator of atrial gene expression. In future work, systematic *in vitro* perturbation of the dosages and timing of expression of established and novel regulators that we identified here (singly and in combinations) will permit a detailed description of the molecular basis for fine patterning of the SAN in a way that would likely be technically unfeasible *in vivo*.

hiPSC-Derived SAN Cells are Specified Shortly after Cardiomyogenesis

The timing and inducing signals for specification of mammalian PCs *in vivo* are not known. In zebrafish and avians, SAN precursors are formed from a heart field that emerges caudal and lateral to the second heart field shortly after cardiac crescent formation. In mouse embryos, a precursor population expressing *Isl1* and *Tbx18* is identifiable in the mouse embryo at E9.0 near the right inflow region closely opposed to the proepicardial organ[28], while timed fate mapping with *Isl1*^{CreEsr} and *Hcn4*^{CreERT2} mice has detected a precursor population as early as E8.0 when the heart tube forms[29,30].

In our hiPSC system, spontaneous electrical activity was present at D10 and in SANCM differentiations as early as D8, with beating activity more rapid than in the ACM or VCM differentiations, suggesting that key events in pacemaker specification occurred shortly after cardiomyocytes are specified, analogous to the timing observed in embryos. In keeping with this result, clustering and pseudotime trajectory analysis of scRNA-seq data from D3, D6, D10, D23, and D34 revealed the likeliest differentiation pathway for PCs, and highlighted several precursor populations that demonstrate increasingly differentiated states until SAN Head, SAN Tail, and transitional cells form clearly resolved clusters by D34.

Closer examination of intermediate states using clustering analysis suggested that pacemaker subtype specification occurs early in the differentiation process. Contrasting expression of *TBX18* and *NKX2-5* consistently emerged in UMAPs for each of the clusters along the SANCM timeline, beginning with D6 *TBX18*$^{+}$ precursors, reinforcing the model of early specification and diversification of pacemaker progenitors[22,31]. By D10, when robust and fast beating was observed, the sinus venosus progenitors had already formed a separate cluster, while PC progenitors had separated into a *TBX18*$^{+}$ domain and a separate *NKX2-5*$^{+}$ domain. This pathway echoes observations from mouse embryos, in which subsets of cells from a broadly *Tbx18*$^{+}$ field at the venous pole downregulate *Tbx18*, upregulate *Nxk2-5*, and form the SAN Tail and transitional cells while persistent Tbx18 expression is required for formation of the SAN Head, as evidenced by the presence of a residual SAN Tail in *Tbx18*$^{-/-}$ mouse embryos with a severely hypoplastic SAN head[32]. Thus far, the specific downstream of targets of *TBX18* at different stages of nodal formation have not been defined. Our hiPSC-derived SANCMs differentiation could be an

attractive system in which to explore the role of *TBX18*, since theoretically large numbers of precursor cells at any stage can be isolated for biochemical and genomic studies.

ISL1 marks the entire posterior SHF and the SAN-forming field, and derivatives of *ISl1*$^{+}$ cells include cardiomyocytes, smooth muscle, epicardial cells, endocardial cells, and fibroblasts[30]. In SHF cardiomyocytes fated to form working myocardium, ISL1 maintains the proliferative progenitor state and then is downregulated as cardiomyocytes differentiate[33]. In contrast, ISL1 expression is maintained in cells fated to form pacemaker myocardium and remains expressed in SAN cells in a gradient from the SAN head (highest expression) to SAN tail (lower expression) and transitional cells (minimal expression), findings that were also observed in SANCMs. A major question for future studies is whether, and if so, how, *ISL1* redistributes its genomic occupancy during the transition from cardiac progenitors to PCs. Integrative multi-omics with motif enrichment analysis strongly suggests that ISL1 is a cell type-specific positive transcriptional regulator that is most active in SAN head cells; the ability to isolate large numbers of these cells offers the possibility of interrogating genomic occupancy of *ISL1* at several stages from cardiac progenitors to PC subtypes and to define its interacting partners specifically in the SAN.

Integration of Omics Data with Human Genetic and Clinical Data for SNP Annotation and Novel Gene Discovery

Inherited variation in heart rhythm phenotypes, including heart rate and propensity to develop atrial fibrillation, are associated with single nucleotide polymorphisms (SNPs) at numerous genetic loci that are commonly presumed to influence traits through linkage to cis-regulatory elements that control gene expression at nearby loci. We found that differentially accessible chromatin in each of the SANCM subtypes significantly overlapped with SNPs that were associated with cardiac traits including heart rate at rest (SAN tail and transitional cells) and heart rate recovery after exercise (SAN head). This finding is a striking confirmation of the hypothesized functional compartmentalization of the SAN, in which migration of the leading pacemaker along the cranial-caudal dimension is driven by changes in autonomic tone that affects SAN head cells disproportionately,

while resting heart rate is driven by mechanisms of impulse generation and transmission that reflect the function of the SAN tail and transitional cells.

The strongest trait association we observed was for atrial fibrillation. Clinically, there is a well- established and strong link between sinus node function and the propensity to develop atrial fibrillation. Because of the existence of common risk factors for both conditions, determining the causal basis for this association has been a long-standing question in the field with major clinical implications. More recent evidence indicates that heart rate determination and atrial fibrillation may have overlapping genetic architectures, although the ability to explore the mechanistic basis for these findings has been limited. By limiting our analysis to regions of accessible chromatin, our analysis highlights the potential for gene discovery and prioritization and raises the possibility for future mechanistic studies on the link between atrial fibrillation and sinus node function.

Conclusion

Our single cell transcriptomic and epigenetic characterization of a novel *in vitro* platform for hiPSC-based differentiation of SAN cardiomyocytes demonstrates reproducilibity, scalability, and fidelity to developmental and physiological pathways important for SAN development and function. These datasets constitute a rich resource on human SAN development and differentiation and the *in vitro* differentiation system could facilitate future applications including studies on SAN gene regulatory networks, SAN physiology, functional genomics of human heart rhythm, drug screening, and tissue engineering.

METHODS

Cell line and maintenance of hiPSC

All differentiations were performed using a commercially available Human episomal iPSC line (ThermoFisher). Culture of hiPSCs was carried out on hESC-Qualified Matrigel (Corning) coated dishes with mTeSR Plus medium (STEMCELL Technologies) and was refreshed every day. Cells were passaged at 80-90% confluence (~every 4 days) using ReLeSR (STEMCELL Technologies) according to manufacturer's instructions.

Differentiation of hiPSCs

Monolayer differentiations of cardiomyocytes were carried out using a modified GiWi strategy (Lian et al 2013). hiPSCs were grown on Matrigel to 90% confluency then harvested as single cell suspension using TrypLE (ThermoFisher) and resuspended in mTeSR Plus containing 10µM ROCK inhibitor Y-27632 (Reprocell). Cells were counted using a Vi-CELL XR Cell Viability Analyzer (Beckman Coulter) and re-plated onto Matrigel coated plates at 15,625-18,230 cells/cm^2 in mTeSR Plus containing 10µM ROCK inhibitor Y-27632 (day -3 of differentiation). Cell plating density was re-optimized every 10 passages or upon a new thaw. At day -2 media was changed to mTeSR Plus. For ventricular cardiomyocytes, at day 0 when cells were 80-90% confluent media was changed to Cardiac Differentiation Media (CDM; RPMI1640 with 25mM HEPES and Glutamax (ThermoFisher) and 1x B27 minus insulin (ThermoFisher)) containing 8µM CHIR99021 (Sigma). On day 2 of differentiation cells were changed to CDM containing 5µM IWP2 (Sigma). At day 4, media was changed to CDM until day 6 when media was switched to Cardiac Maintenance Media (CMM; RPMI1640 with 25mM HEPES and Glutamax (ThermoFisher) and 1x B27 supplement (ThermoFisher). Media was changed every 2 days until day 20. On day 20 cells were split 1:4 in preparation for metabolic selection. Cells were washed with TrypLE for 5 minutes at room temperature then digested into single cell suspension using prewarmed Accumax (Sigma) for 20-30 minutes at 37°C. Digestion was quenched using CMM containing 20% Knock-out serum replacement (ThermoFisher) and 10µM ROCK inhibitor Y-27632 and cells collected by centrifugation at 200xg for 5 minutes. Cells were then resuspended in CMM containing 20% Knock-out serum replacement and 10µM ROCK inhibitor Y-27632 and plated onto new Matrigel coated dishes at 25% the original confluence (1:4 split). 24 hours later (day 21) media was changed to CMM. At day 23 media was changed to Cardiomyocyte Selection Media (CSM; RPMI1640 with Glutamine and No glucose (ThermoFisher), 5mM Sodium DL-lactate solution (Sigma) and 0.5mg/ml Human Serum Albumin (Sigma)). CSM was changed every 2 days until day 31 when cells were switched back to CMM. Cells were maintained in CMM (media changed every 2 days) until cells were either frozen (day 34) or used for analysis.

For atrial cardiomyocytes, the same protocol was followed except for the following addition. On day 3 of differentiation, 1µM Retinoic Acid (RA; Sigma) was spiked into the CDM containing IWP2. For SAN cardiomyocytes the ventricular protocol was following with the following modifications. At day 3, 2.5ng/ml BMP4 (R&D Systems), 5.4µM SB431542 (Tocris) and 0.5µM RA were spiked into the CDM containing IWP2. On day 4, media was replaced with CDM containing 240nM PD173074 (Tocris).

Quantitative real-time RT-PCR

Total RNA was extracted from cells using RNeasy mini kit (Qiagen) according to the manufacturer's instructions. Purified RNA was subjected to reverse transcription as described in the SuperScript IV VILO with ezDNase enzyme kit (ThermoFisher). Following cDNA synthesis, expression level of the genes was quantified by quantitative Real-Time PCR (qPCR) using TaqMan Fast Advanced Master Mix (ThermoFisher) on a QuantStudio 7 Flex Real-Time PCR system (ThermoFisher). The quantification was analysed using the C_T (threshold cycle) values. The expression of the target genes were normalized to *GAPDH.* Expression was then calculated using the $2^{-\Delta\Delta Ct}$ method and graphed relative to ventricular cardiomyocytes.

Immunofluorescence staining

Cells were cultured in CellCarrier-96 Ultra Microplates (Perkin Elmer) coated with 50µg/ml fibronectin (Sigma) and 0.1% Gelatin (STEMCELL Technologies). Cells were washed with PBS then fixed with 4% PFA for 20 min at room temperature and washed again with PBS. Cells were then blocked and permeabilized with 0.1% Triton X-100 and 5% donkey serum in PBS for 1 hour at room temperature on a rotator. Primary antibodies diluted in blocking/permeabilization buffer were added and incubated at 4°C overnight on a shaker at 3000 rpm. Cells were washed 3 times for 3 minutes in PBS at room temperature on a shaker at 3000 rpm. Secondary antibodies diluted in PBS with 5% donkey serum were added and incubated at room temperature for 1 hour shaking at 3000 rpm then followed by 2x3 minute washes in PBS with shaking. The cell nuclei were counterstained with Hoesht 33342 (1:2000; Thermo Fisher) for 10 minutes with shaking and then washed 2x3 minutes with shaking in PBS. Cells were imaged with an Opera

Phenix High Content Screening System (Perkin Elmer) using Harmony software and analyzed using Columbus software (Perkin Elmer).

The following primary antibodies were used: mouse anti-Cardiac Troponin T (ThermoFisher; 1:200), rabbit anti-Cardiac Troponin T (Abcam; 1:200), mouse anti-ISL1/2 (DSHB; 1:200), rabbit anti-NKX2.5 (Cell Signaling; 1:200), rabbit anti-HCN4 (Alomone; 1:200) and mouse anti-SHOX2 (Abcam; 1:200). The following secondary antibodies were used: donkey anti-mouse Alexa Fluor 488 (ThermoFisher; 2µg/ml) and donkey anti-rabbit Alexa Fluor 555 (ThermoFisher; 2µg/ml).

Imaging of Voltage-Sensitive Dye

Voltage imaging of VCMs and SANCMs was performed by adding FluoVolt membrane potential dye (ThermoFisher) to 96 well-plates seeded with 100k cells/well. Briefly, FluoVolt was mixed 1:20 with PowerLoad concentrate, and diluted 100x with FluoroBrite DMEM (ThermoFisher). 100x water-soluble Probenecid (ThermoFisher) was then added to achieve a final concentration of 1x. After washing with FluoroBrite DMEM, cells were incubated for 5 min at RT with the dye solution. The dye was then removed and replaced with FluoroBrite DMEM with 1x Probenecid. The cell plate was then placed inside the culture chamber of an iMX4 microscope (Molecular Devices) and equilibrated for 5 minutes. Time lapse images were then acquired for 5 seconds per site at 100 fps, using a 10x objective. For Zatebradine measurements, cells were prepared as described above then treated with 0, 0.1, 0.3, 1 or 3 µM Zatebradine (Tocris), incubated for 5 minutes then imaged. The images (5 fields per well, 4 wells per treatment) were then analyzed using a custom Matlab script that extracted individual voltage traces for each cell in the field and calculated electrophysiological parameters including beating rate, amplitude, and action potential duration at 20%, 50% and 90% repolarization. All parameters were averaged and compared between groups using a student's T-test after each distribution passed a normality test.

scRNA-seq data analysis

Initial processing of scRNA-seq data was done with the Cell Ranger Pipeline (https://support.10xgenomics.com/single-cell-geneexpression/software/pipelines/latest/what-is-cell-ranger, v.6.0.0) by first running cellranger mkfastq to demultiplex the bcl files and then running cellranger count with 10x Genomics' pre-built Cell Ranger reference GRCh38-2020-A_build. After running Cell Ranger, the filtered_feature_bc_matrix produced by Cell Ranger was read into R (v.4.0.4) with the Seurat (v.4.3.0) function Read10X [34]. scDblFinder (v.1.2.0) was run for each sample for detecting doublets [35]. Cells classified as doublets were not enriched in any clusters identified in the downstream clustering analysis and thus retained. Cells from all samples were merged into a single Seurat object and analyzed separately for each dataset.

For the analysis of cells of Day 34 datasets (ACM, VCM, and SANCM cultures), cell barcodes were filtered based on the number of genes per cell (between 1,000 and 9,000), unique molecular identifiers (UMIs) per cell (more than 1500), and percentage of mitochondrial reads per cell (less than 50%). The filtered cell number used for subsequent analysis was 20,712 cells for the Day 34 SANCM culture, 21,676 cells for the Day 34 ACM culture, 21,934 cells for the Day 34 ACM culture, 102,496 cells for the SANCM time-course Day 3 to Day 34 cultures, respectively.

For the analysis of SANCM time-course datasets (Day 3 to Day 34 SANCM cultures), the following criteria was applied: number of genes per cell between 2,000 and 10,000, UMIs per cell (between 5,000 and 80,000), percentage of mitochondrial reads per cell (less than 10% for Day3, Day 4, and Day 6 datasets; less than 15% for Day 10 and Day 23 datasets; less than 40% for Day 34). Read counts were normalized using Seurat's sctransform method. Cell-cycle scoring was calculated with the CellCycleScoring algorithm from Seurat using cell-cycle-related genes and cell cycle effects were regressed out (vars.to.regress = c("S.Score", "G2M.Score")). The 5000 most variable genes were identified for subsequent analysis.

For the analysis of Day 34 datasets and SANCM time-course datasets, principal component analysis (PCA) was performed using the RunPCA function and the top 40 principal components (PCs) were selected. UMAP was computed using the RunUMAP function and cells were clustered using a k-nearest neighbour graph and the Louvain

algorithm with the FindNeighbors and FindClusters functions. A resolution of 0.6 and 1.0 was used for Day 34 datasets and time-course datasets, respectively. Expression of canonical marker genes and enriched pathways in the marker genes (described below) in the resulting clusters were then used to label clusters.

For the sub-clustering analysis of Day 34 SANCM, ACM, and VCM cultures, replicates were integrated using the Seurat integration procedure. When running FindIntegrationAnchors and IntegrateData, the normalization.method parameter was set to the “SCT” using 30 dimensions and 5000 features. For dimensionality reduction, the integrated expression matrix was used to compute PCs by RunPCA. The top 40 PCs were selected for UMAP visualizations and clustering analysis. The cells were then clustered using Seurat’s FindNeighbors and FindClusters with a resolution of 0.5 for the Day 34 SANCM dataset, 0.4 for the Day 34 VCM dataset, and 0.3 for the Day 34 ACM dataset, respectively. The clusters were manually annotated based on canonical markers and enriched pathways.

For the sub-clustering analysis of the Day 34 SANCM dataset, cells were first separated into 20 clusters as described above. Eleven clusters were removed due to enrichment of cell cycle genes (3 clusters), low gene count (4 clusters), high percentage of mitochondrial reads (2 clusters), enrichment of genes in cell stress related pathways (1 cluster), or without consistent expression of canonical markers of any cell type (3 clusters). Cells in the retained clusters were normalized and integrated again using the same pipeline. Dimensionality reduction was recomputed, and clustering analysis was performed with a resolution of 0.8.

For the sub-clustering analysis of SAN head and tail cells, the three clusters identified as SAN head and tail cells (cluster 2, 0, and 3 in Fig. 3C) were subset and analyzed separately. Normalization was performed by Seurat’s sctransform method with the 3,000 most variable genes and regressing out cell cycle effects, and batch effect was removed using Harmony (v. 0.1.0)[36].Cluster identification and UMAP reduction were conducted as above, except that a resolution of 0.1 was used for the clustering. For the sub-clustering of clusters 28, 5, and 14 in the SANCM time course datasets (Fig. 5A), the same pipeline was used except that a resolution of 0.3, 0.2, and 1.0 were used for these clusters, respectively.

For each dataset, the FindAllMarkers and FindMarkers functions were performed after normalizing the expression counts with Seurat's "LogNormalize" method to identify the marker genes for each cluster (min.pct = 0.25, logfc.threshold = 0.25) and intercluster differentially expressed genes (min.pct = 0.25, Padj < 0.05, logfc.threshold = 0.5 for SANCM time-course datasets and 0.25 for Day 34 datasets) via the Wilcoxon rank sum test. Pathway analysis of marker genes and differentially expressed genes was conducted with MetaScape (v3.5) [37].

Trajectory Analysis

PAGA [38] implemented in scanpy (v.1.9.1[39]) was used to compute the connectivites between clusters (sc.tl.paga) and compute the PAGA graph after denoising with diffusion map. Cell differentiation lineages were constructed manually based on the similarities between clusters, timepoints and annotation of the clusters. For each lineage, diffusion map and diffusion pseudotime were computed using the R package destiny (v.3.2.0)[40].

Integration of publicly available scRNA-seq datasets

Two preprocessed scRNA-seq datasets were downloaded from the Gene Expression Omnibus (GEO) (accession code GSE189782[11] and GSE193723[41]) and processed using Seurat as described in the studies. We used two methods for integration of these datasets with our Day 34 SANCM scRNA-seq data. First, we performed reference mapping to project the cells in the two public datasets onto the UMAP structure of our Day 34 SANCM scRNA-seq data according to Seurat's "Mapping and annotating query datasets" tutorial (https://satijalab.org/seurat/articles/integration_mapping.html). Specifically, the FindTransferAnchors function was used to find a set of anchors between the reference and query object with the top 40 PCs and "SCT" normalization. These anchors were then passed into the MapQuery function to project the query data onto the UMAP embedding of the reference. Second, we jointly analyzed and integrated each public dataset with our Day 34 SANCM dataset separately using the Seurat integration procedure. Read counts were normalized using Seurat's sctransform method and cell cycle scores and percent of mitochondrial reads were regressed out. When running FindIntegrationAnchors and IntegrateData, the normalization.method parameter was set

to the “SCT” using 30 dimensions and 3000 features. The top 40 PCs were selected for UMAP visualizations and clustering analysis.

scATAC-seq data analysis

Initial processing of the Day 34 SANCM scATAC-seq data was performed using Cell Ranger ATAC (https://support.10xgenomics.com/single-cell-atac/software/pipelines/latest/what-is-cell-ranger-atac, v.2.0.0) by first running cellranger-atac mkfastq to demultiplex the bcl files into FASTQ files and then running cellranger-atac count to generate scATAC fragments files with 10x Genomics’ pre-built Cell Ranger reference GRCh38-2020-A_build and default parameters.

These fragments files were loaded into R (v.4.0.4) using the createArrowFiles function in ArchR (v.1.0.1) [42]. Quality control metrics were computed for each cell, and cells with TSS enrichments less than 4 and number of unique fragments less than 1,000 were filtered out for all samples. The number of cells retained was 38,744 (ranging from 10,565 to 15,823). Doublets were detected by AMULET (v.1.1) [43] for each sample. Cells classified as doublets were retained due to lack of enrichment in any clusters identified in the subsequent clustering analysis.

After generating arrow files for each sample, an ArchR project containing all samples was created. As part of construction of the arrow files, a tile matrix consisting of reads in 500-bp tiles was constructed. This tile matrix was used as input to compute an iterative latent semantic indexing (LSI) dimensionality reduction using the addIterativeLSI function in ArchR with a total of 2 iterations, a clustering resolution of 0.2 following the first iteration, 50,000 variable features, 30 dimensions and sampling 10,000 cells. Harmony (v. 0.1.0) [36] was applied to the dataset to correct for the batch effects. Using the Harmony-corrected dimension reduction, clustering was performed using ArchR’s addClusters with a resolution of 0.45. We next ran addUMAP on the Harmony-corrected dimensionality reduction with 30 nearest neighbors and a minimum distance of 0.5. Gene activity scores computed by ArchR base on the accessibility within and around a given gene body were examined for the known marker genes. Clusters with less than 34 cells consisted mainly of cells from only a subset of the samples and were removed from the subsequent analysis. One cluster containing about 3000 cells that could not be

confidently assigned to one cell type and probably constitute poor quality nuclei was also removed from further analysis.

For sub-clustering of SAN head and tail cells, scATAC-seq clusters identified as SAN head and tail cells were subset and used to recompute iterative LSI dimensionality reduction as described above. Batch correction, cluster identification, and UMAP reduction were also performed as above, except that a resolution of 0.2 was used for the clustering.

Integration of scATAC-seq and scRNA-seq data

Day 34 SANCM scRNA-seq gene expression counts were integrated with scATAC-seq data with addGeneIntegrationMatrix in ArchR as a constrained integration, grouping GC B cell clusters, other B cell clusters, and non–B cell clusters together during addGeneIntegrationMatrix to the following groups: SAN head, SAN tail, SAN transitional, ACM-like transitional, Sinus Venosus, proepicardial and neuronal cells. The output of the integration step resulted in snATAC-seq cells having both a chromatin accessibility and a gene expression profile. Accessibility gene scores and transferred RNA expression counts were imputed with addImputeWeights.

Cell-type-specific peak and TF motif enrichment

Pseudobulk group coverages of cell type clusters were calculated with the ‘addGroupCoverages’ function and used for peak calling using the ‘addReproduciblePeakSet’ function in ArchR. A background peak set controlling for total accessibility and GC content was generated using addBgdPeaks for TF enrichment analyses. Cell type–specific marker peaks and differentially accessible peaks between clusters were identified with ‘getMarkerFeatures’ with the Wilcoxon test (maxCells = 10,000, FDR ≤ 0.05, and Log2FC ≥ 0.5 for marker peaks, and maxCells =6,000, FDR ≤ 0.01, and |Log2FC| ≥ 1 for differential accessible peaks). The enriched motifs for marker peaks of each cluster and differential accessible peaks were predicted using the ‘addMotifAnnotations’ function in ArchR based on the cisbp motif set. Chromvar was run with addDeviationsMatrix to calculate enrichment of chromatin accessibility at different

TF motif sequences in single cells. To identify correlations between the gene expression and TF activity, the GeneIntegrationMatrix and the Chromvar deviations (MotifMatrix) were correlated using correlateMatrices. A correlation of greater than 0.5 and an adjusted p-value less than 0.01 were used to determine whether TF expression and activity were positively correlated. “Peak-to-gene links” were calculated using correlations between peak accessibility and integrated scRNA-seq expression data using addPeak2GeneLinks with the parameter ‘maxDist = 1.5e6' and getPeak2GeneLinks in ArchR. We further visualized the peak to gene links using the ‘plotBrowserTrack’ function in ArchR.

Stratified linkage disequilibrium (LD) score regression

We used the LDSC package (v1.0.1) [44] to estimate genome-wide GWAS enrichment for a variety of phenotypes within the cell type-specific scATAC-seq peaks. We first downloaded GWAS summary statistics for: atrial fibrillation, resting heart rate, heart rate increase in response to exercise, heart rate response to recovery post exercise (20 sec) (the GWAS catalog https://www.ebi.ac.uk/gwas/; accessions codes GCST006414, GCST007609, GCST005845, and GCST005847); height (https://rpubs.com/leaknielsen/1027689); diastolic blood pressure, systolic blood pressure, years of education, smoking status, auto immune traits, asthma, dermatologic diseases, high cholesterol, type 2 diabetes, age at menarche, BMI (https://alkesgroup.broadinstitute.org/UKBB/); schizophrenia, major depression disorder, Alzheimer’s disease (https://pgc.unc.edu/for-researchers/download-results/; pubMedIDlink 25056061, 29700475, 30617256); coronary artery disease, QT prolongation, LV stroke vol. indexed, sscending aorta diameter index, LV max. area index, LV min. area index, pulmonary artery:aorta ratio, RA fractional area change, RA max. area index, RA min. area index, RV end diastolic vol. index, RV ejection fraction, RV end systolic vol. index, P-wave duration, PR interval, QRS duration, QTc interval, RR interval, heart failure, LV ejection fraction (https://personal.broadinstitute.org/ryank/; Aragam_2022_CARDIoGRAM_CAD_GWAS.zip, Nauffal_2022_QT_GWAS_SAIGE.zip, Pirruccello_2022_UKBB_HeartStructures.zip, Choi2021_TOPMed_freeze6.zip, HERMES_Jan2019_HeartFailure_summary_data.txt.zip, MRI_lvef_filtered.zip); IBD (https://www.dropbox.com/s/ttuc6s7tv26voq3/iibdgc-trans-ancestry-filtered-summary-

stats.tgz?dl=0); total cholesterol (http://csg.sph.umich.edu/abecasis/public/lipids2013/jointGwasMc_TC.txt.gz). We then used the provided munge_sumstats.py script to convert these GWAS summary statistics to a format compatible with LDSC.

Using all the ATAC-seq peaks called within each cluster, we generated the annotation-specific partitioned LD score files for each cluster separately according to the "Partitioned LD scores" section of the LD score estimation tutorial (https://github.com/bulik/ldsc/wiki/LD-Score-Estimation-Tutorial). We downloaded the list of 1,154,611 candidate cis-regulatory elements (cCREs) for 222 distinct cell types from the Human Enhancer Atlas (http://catlas.org/humanenhancer/#!/)[45] and used them as background annotations. We lifted over peak coordinates from hg38 to hg19 for both Day 34 SANCM ATAC-seq peaks and background peaks using CrossMap (v.0.6.3) [46] before computing annotation-specific LD scores. We then used these hg19 bed files to make annotation files for each cell type. For each trait, we used LD score regression to estimate coefficient p value for each cell type relative to the background annotations according to the cell-type-specific analysis tutorial (https://github.com/bulik/ldsc/wiki/Cell-type-specific-analyses) and used the Benjamini-Hochberg correction for multiple testing.

Integration of atrial fibrillation GWAS and scATAC-seq data

Summary statistics were downloaded from the GWAS catalog for two previous studies for atrial fibrillation (accessions codes GCST006414 [47] and GCST006061[48]) and consolidated by removing one copy of the redundant SNPs in both studies with larger p-value. All the SNPs were then assigned to their nearest genes based on their coordinates. Bedtools (v.2.30.0)[49] was used to intersect the SNP coordinates with marker peaks for SAN head, tail and transitional cells separately and also the union of all the peaks identified in these clusters. To calculate the customized genome-wide significance threshold for the SNPs within the ATAC peaks, the SNPclip tool of LDlink (https://ldlink.nih.gov/?tab=home) [50] was used to prune the list of SNPs in the marker peaks of each cell type by linkage disequilibrium with the CEU population (R^2 0.1 and MAF 0.01) and the GRCh38 genome build. The p-value threshold was then calculated through dividing 0.05 by the number of SNPs left after pruning (0.05/11573 = 4.32e-06

for SAN head, 0.05/8921 = 5.60e-06 for SAN tail, and 0.05/13351 = 3.75e-06 for SAN transitional cells). To identify the 'novel' genes associated with atrial fibrillation, the SNPs in the marker peaks with p-value between the traditional GWAS cutoff 5e-08 and the customized p-value threshold were selected, and a list of their nearest genes was obtained. Only the genes which were not assigned with a genome-wide significant SNP (p-value < 5e-08), whose assigned SNPs were not in high LD ($r^2 > 0.8$) with a genome-wide significant SNP, and which were not associated with atrial fibrillation in the GWAS catalog were considered as novel findings.

Acknowledgements. The authors wish to thank

Sources of Funding. This work was supported by a grant from the NIH (DP2HL152425 to V.V.) and a philanthropic gift from the Susan and Matt Ryan Foundation.

REFERENCES

1 Mangoni, M. E. & Nargeot, J. Genesis and regulation of the heart automaticity. *Physiol Rev* **88**, 919-982, doi:88/3/919 [pii]

10.1152/physrev.00018.2007 (2008).

2 Bleeker, W. K., Mackaay, A. J., Masson-Pevet, M., Bouman, L. N. & Becker, A. E. Functional and morphological organization of the rabbit sinus node. *Circ Res* **46**, 11-22 (1980).

3 Liu, J., Dobrzynski, H., Yanni, J., Boyett, M. R. & Lei, M. Organisation of the mouse sinoatrial node: structure and expression of HCN channels. *Cardiovasc Res* **73**, 729-738, doi:10.1016/j.cardiores.2006.11.016 (2007).

4 Unudurthi, S. D., Wolf, R. M. & Hund, T. J. Role of sinoatrial node architecture in maintaining a balanced source-sink relationship and synchronous cardiac pacemaking. *Front Physiol* **5**, 446, doi:10.3389/fphys.2014.00446 (2014).

5 Boyett, M. R., Honjo, H. & Kodama, I. The sinoatrial node, a heterogeneous pacemaker structure. *Cardiovasc Res* **47**, 658-687, doi:10.1016/s0008-6363(00)00135-8 (2000).

6 Devalla, H. D. *et al.* Atrial-like cardiomyocytes from human pluripotent stem cells are a robust preclinical model for assessing atrial-selective pharmacology. *EMBO Mol Med* **7**, 394-410, doi:10.15252/emmm.201404757 (2015).

7 Funakoshi, S. *et al.* Generation of mature compact ventricular cardiomyocytes from human pluripotent stem cells. *Nat Commun* **12**, 3155, doi:10.1038/s41467-021-23329-z (2021).

8 Protze, S. I. *et al.* Sinoatrial node cardiomyocytes derived from human pluripotent cells function as a biological pacemaker. *Nat Biotechnol* **35**, 56-68, doi:10.1038/nbt.3745 (2017).
9 Chou, P. C. *et al.* Fibroblasts Drive Metabolic Reprogramming in Pacemaker Cardiomyocytes. *Circ Res* **131**, 6-20, doi:10.1161/CIRCRESAHA.121.320301 (2022).
10 Hou, X. *et al.* Chemically defined and small molecules-based generation of sinoatrial node-like cells. *Stem Cell Res Ther* **13**, 158, doi:10.1186/s13287-022-02834-y (2022).
11 Wiesinger, A. *et al.* A single cell transcriptional roadmap of human pacemaker cell differentiation. *Elife* **11**, doi:10.7554/eLife.76781 (2022).
12 Lee, J. H., Protze, S. I., Laksman, Z., Backx, P. H. & Keller, G. M. Human Pluripotent Stem Cell-Derived Atrial and Ventricular Cardiomyocytes Develop from Distinct Mesoderm Populations. *Cell Stem Cell* **21**, 179-194 e174, doi:10.1016/j.stem.2017.07.003 (2017).
13 Cyganek, L. *et al.* Deep phenotyping of human induced pluripotent stem cell-derived atrial and ventricular cardiomyocytes. *JCI Insight* **3**, doi:10.1172/jci.insight.99941 (2018).
14 Lian, X. *et al.* Directed cardiomyocyte differentiation from human pluripotent stem cells by modulating Wnt/β-catenin signaling under fully defined conditions. *Nat Protoc* **8**, 162-175, doi:10.1038/nprot.2012.150 (2013).
15 Tohyama, S. *et al.* Distinct metabolic flow enables large-scale purification of mouse and human pluripotent stem cell-derived cardiomyocytes. *Cell Stem Cell* **12**, 127-137, doi:10.1016/j.stem.2012.09.013 (2013).
16 Wiesinger, A., Boink, G. J. J., Christoffels, V. M. & Devalla, H. D. Retinoic acid signaling in heart development: Application in the differentiation of cardiovascular lineages from human pluripotent stem cells. *Stem Cell Reports* **16**, 2589-2606, doi:10.1016/j.stemcr.2021.09.010 (2021).
17 Vedantham, V., Galang, G., Evangelista, M., Deo, R. C. & Srivastava, D. RNA Sequencing of Mouse Sinoatrial Node Reveals an Upstream Regulatory Role for Islet-1 in Cardiac Pacemaker Cells. *Circulation research* **116**, 797-803, doi:10.1161/CIRCRESAHA.116.305913 (2015).
18 Galang, G. *et al.* ATAC-Seq Reveals an Isl1 Enhancer That Regulates Sinoatrial Node Development and Function. *Circ Res* **127**, 1502-1518, doi:10.1161/CIRCRESAHA.120.317145 (2020).
19 van Eif, V. W. W. *et al.* Transcriptome analysis of mouse and human sinoatrial node cells reveals a conserved genetic program. *Development* **146**, doi:10.1242/dev.173161 (2019).
20 Wiese, C. *et al.* Formation of the sinus node head and differentiation of sinus node myocardium are independently regulated by Tbx18 and Tbx3. *Circulation Research* **104**, 388-397, doi:10.1161/CIRCRESAHA.108.187062 (2009).
21 Wakimizu, T. *et al.* SHOX2 refines the identification of human sinoatrial nodal cell population in the in vitro cardiac differentiation. *Regen Ther* **21**, 239-249, doi:10.1016/j.reth.2022.07.012 (2022).

22 Ren, J. *et al.* Canonical Wnt5b Signaling Directs Outlying Nkx2.5+ Mesoderm into Pacemaker Cardiomyocytes. *Dev Cell* **50**, 729-743 e725, doi:10.1016/j.devcel.2019.07.014 (2019).
23 Jung, J. J. *et al.* Programming and isolation of highly pure physiologically and pharmacologically functional sinus-nodal bodies from pluripotent stem cells. *Stem Cell Reports* **2**, 592-605, doi:10.1016/j.stemcr.2014.03.006

S2213-6711(14)00085-X [pii] (2014).
24 Yan, Y., Liu, F., Dang, X., Zhou, R. & Liao, B. TBX3 induces biased differentiation of human induced pluripotent stem cells into cardiac pacemaker-like cells. *Gene Expr Patterns* **40**, 119184, doi:10.1016/j.gep.2021.119184 (2021).
25 Gorabi, A. M. *et al.* TBX18 transcription factor overexpression in human-induced pluripotent stem cells increases their differentiation into pacemaker-like cells. *J Cell Physiol* **234**, 1534-1546, doi:10.1002/jcp.27018 (2019).
26 Goodyer, W. R. *et al.* Transcriptomic Profiling of the Developing Cardiac Conduction System at Single-Cell Resolution. *Circulation Research* **125**, 379-397, doi:10.1161/CIRCRESAHA.118.314578 (2019).
27 Landi, S. *et al.* Lack of the transcription factor Nfix causes tachycardia in mice sinus node and rats neonatal cardiomyocytes. *Acta Physiol (Oxf)*, e13981, doi:10.1111/apha.13981 (2023).
28 Mommersteeg, M. T. *et al.* The sinus venosus progenitors separate and diversify from the first and second heart fields early in development. *Cardiovasc Res* **87**, 92-101, doi:10.1093/cvr/cvq033 (2010).
29 Liang, X. *et al.* HCN4 dynamically marks the first heart field and conduction system precursors. *Circ Res* **113**, 399-407, doi:CIRCRESAHA.113.301588 [pii]

10.1161/CIRCRESAHA.113.301588 (2013).
30 Sun, Y. *et al.* Islet 1 is expressed in distinct cardiovascular lineages, including pacemaker and coronary vascular cells. *Dev Biol* **304**, 286-296, doi:10.1016/j.ydbio.2006.12.048 (2007).
31 Bressan, M., Liu, G. & Mikawa, T. Early mesodermal cues assign avian cardiac pacemaker fate potential in a tertiary heart field. *Science* **340**, 744-748, doi:science.1232877 [pii]

10.1126/science.1232877 (2013).
32 Wiese, C. *et al.* Formation of the sinus node head and differentiation of sinus node myocardium are independently regulated by Tbx18 and Tbx3. *Circ Res* **104**, 388-397, doi:10.1161/CIRCRESAHA.108.187062 (2009).
33 Cai, C. L. *et al.* Isl1 identifies a cardiac progenitor population that proliferates prior to differentiation and contributes a majority of cells to the heart. *Dev Cell* **5**, 877-889, doi:S1534580703003630 [pii] (2003).
34 Hao, Y. *et al.* Integrated analysis of multimodal single-cell data. *Cell* **184**, 3573-3587 e3529, doi:10.1016/j.cell.2021.04.048 (2021).
35 Germain, P. L., Lun, A., Garcia Meixide, C., Macnair, W. & Robinson, M. D. Doublet identification in single-cell sequencing data using scDblFinder. *F1000Res* **10**, 979, doi:10.12688/f1000research.73600.2 (2021).
36 Korsunsky, I. *et al.* Fast, sensitive and accurate integration of single-cell data with Harmony. *Nat Methods* **16**, 1289-1296, doi:10.1038/s41592-019-0619-0 (2019).

37 Zhou, Y. *et al.* Metascape provides a biologist-oriented resource for the analysis of systems-level datasets. *Nat Commun* **10**, 1523, doi:10.1038/s41467-019-09234-6 (2019).
38 Wolf, F. A. *et al.* PAGA: graph abstraction reconciles clustering with trajectory inference through a topology preserving map of single cells. *Genome Biol* **20**, 59, doi:10.1186/s13059-019-1663-x (2019).
39 Wolf, F. A., Angerer, P. & Theis, F. J. SCANPY: large-scale single-cell gene expression data analysis. *Genome Biol* **19**, 15, doi:10.1186/s13059-017-1382-0 (2018).
40 Angerer, P. *et al.* destiny: diffusion maps for large-scale single-cell data in R. *Bioinformatics* **32**, 1241-1243, doi:10.1093/bioinformatics/btv715 (2016).
41 Han, Y. *et al.* SARS-CoV-2 Infection Induces Ferroptosis of Sinoatrial Node Pacemaker Cells. *Circ Res* **130**, 963-977, doi:10.1161/CIRCRESAHA.121.320518 (2022).
42 Granja, J. M. *et al.* ArchR is a scalable software package for integrative single-cell chromatin accessibility analysis. *Nat Genet* **53**, 403-411, doi:10.1038/s41588-021-00790-6 (2021).
43 Thibodeau, A. *et al.* AMULET: a novel read count-based method for effective multiplet detection from single nucleus ATAC-seq data. *Genome Biol* **22**, 252, doi:10.1186/s13059-021-02469-x (2021).
44 Finucane, H. K. *et al.* Partitioning heritability by functional annotation using genome-wide association summary statistics. *Nat Genet* **47**, 1228-1235, doi:10.1038/ng.3404 (2015).
45 Zhang, K. *et al.* A single-cell atlas of chromatin accessibility in the human genome. *Cell* **184**, 5985-6001 e5919, doi:10.1016/j.cell.2021.10.024 (2021).
46 Zhao, H. *et al.* CrossMap: a versatile tool for coordinate conversion between genome assemblies. *Bioinformatics* **30**, 1006-1007, doi:10.1093/bioinformatics/btt730 (2014).
47 Nielsen, J. B. *et al.* Biobank-driven genomic discovery yields new insight into atrial fibrillation biology. *Nat Genet* **50**, 1234-1239, doi:10.1038/s41588-018-0171-3 (2018).
48 Roselli, C. *et al.* Multi-ethnic genome-wide association study for atrial fibrillation. *Nat Genet* **50**, 1225-1233, doi:10.1038/s41588-018-0133-9 (2018).
49 Quinlan, A. R. & Hall, I. M. BEDTools: a flexible suite of utilities for comparing genomic features. *Bioinformatics* **26**, 841-842, doi:10.1093/bioinformatics/btq033 (2010).
50 Machiela, M. J. & Chanock, S. J. LDlink: a web-based application for exploring population-specific haplotype structure and linking correlated alleles of possible functional variants. *Bioinformatics* **31**, 3555-3557, doi:10.1093/bioinformatics/btv402 (2015).

Figure 1: Generation and characterization of hiPSC derived Cardiomyocyte-like subtypes. (A) Schematic showing differentiation protocols for generation of hiPSC derived Cardiomyocyte-like subtypes. (B-F) qPCR for (B) pan-cardiac, (C) ventricular, (D) atrial, (E) pacemaker and (F) ion channel related genes in hiPSC derived Cardiomyocyte subtypes. (G) Immunocytochemistry of ISL1, SHOX2 and NKX2-5 expression (green) in hiPSC derived VCMs and SANCMs stained with TNNT2 (red) and Hoescht (blue). (H) Quantification of nuclear signal intensities from G in two replicates. Dotted lines indicate threshold cutoffs for quantification. (I) Representative traces, cycle length, amplitude and ADP50 measurements recorded from VCMs and SANCMs using FluoVolt. (J) Dose response of SANCMs treated with the HCN channel blocker Zatebradine. Significance was determined using one-way ANOVA with multiple comparisons tests. * $p<0.05$ ** $p<0.01$ *** $p<0.001$ **** $p<0.0001$

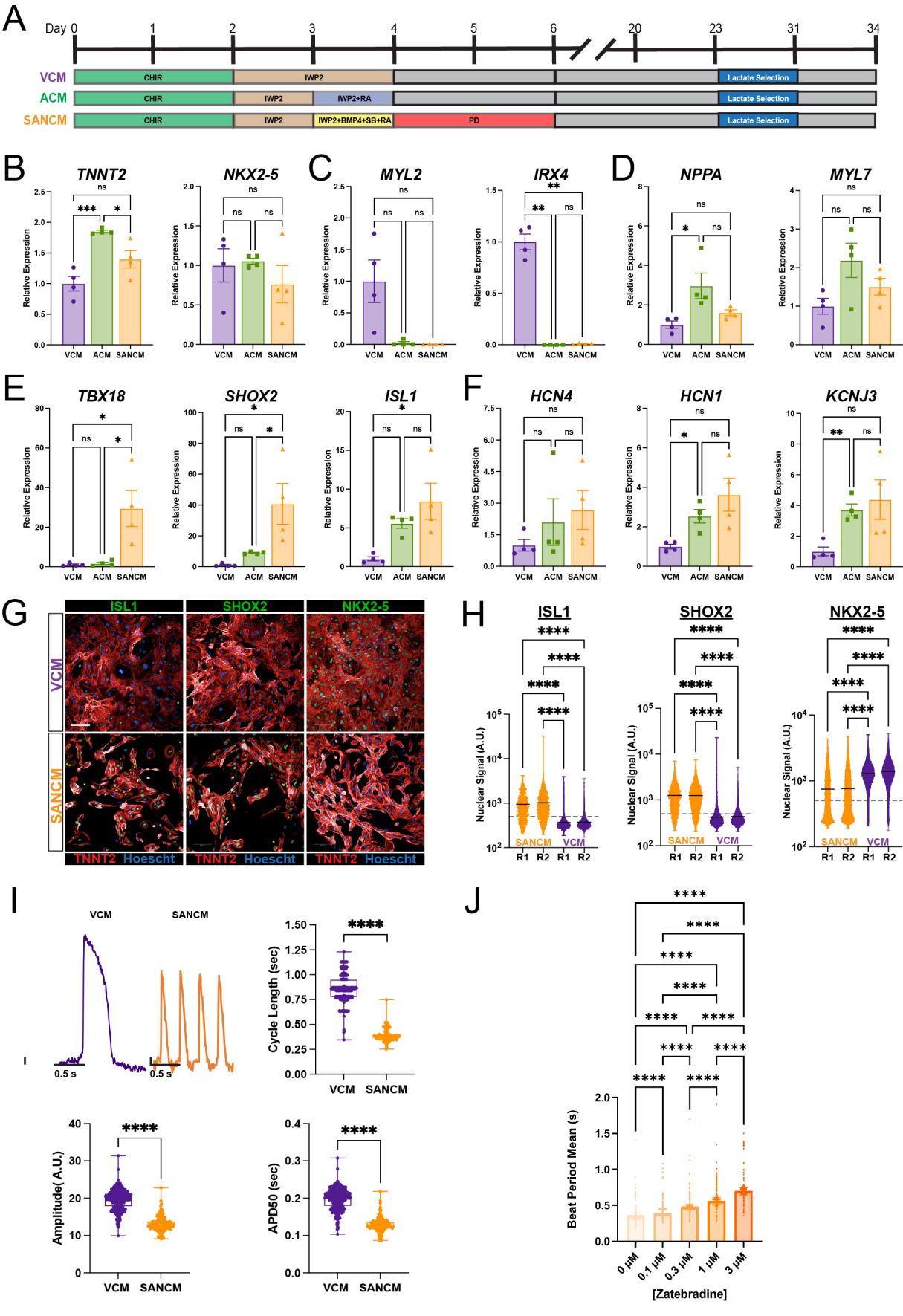
A
Day 0
1
2
3
4
5
6
20
23
31
34
VCM
CHIR
IWP2
Lactate Selection
ACM
CHIR
IWP2
IWP2+RA
Lactate Selection
SANCM
CHIR
IWP2
IWP2+BMP4+SB+RA
PD
Lactate Selection
B
TNNT2
NKX2-5
C
MYL2
IRX4
D
NPPA
MYL7
E
TBX18
SHOX2
ISL1
F
HCN4
HCN1
KCNJ3
Relative Expression
VCM
ACM
SANCM
ns
*
**
***
G
ISL1
SHOX2
NKX2-5
VCM
SANCM
TNNT2 Hoescht
H
ISL1
SHOX2
NKX2-5
Nuclear Signal (A.U.)
SANCM
VCM
R1
R2
****
I
VCM
SANCM
0.5 s
Cycle Length (sec)
Amplitude(A.U.)
APD50 (sec)
J
Beat Period Mean (s)
0 μM
0.1 μM
0.3 μM
1 μM
3 μM
[Zatebradine]

Figure 2: scRNA-seq of day 34 hiPSC derived VCMs, ACMs and SANCMs. (A) UMAP visualization of transcriptionally distinct cell populations from different CM differentiations. (B) UMAP embedding showing annotated cell clusters. (C) Unsupervised clustering of cells in the UMAP space. Cells of clusters 2, 7, 9, and 15 represent VCMs, 0, 6, 8, and 12 are ACMs and cluster 1 are SANCMs. (D) Dot plot showing the top 10 marker genes for VCM, ACM and SANCMs clusters in (C). (E) Feature plots (top) and violin plots (bottom) showing expression of selected canonical genes used to annotate SANCMs. (F) Heatmap of differentially expressed genes between ACMs and SANCMs. (G) Bar plot showing the top 20 enriched pathways in SANCMs vs ACMs based on differentially expressed genes.

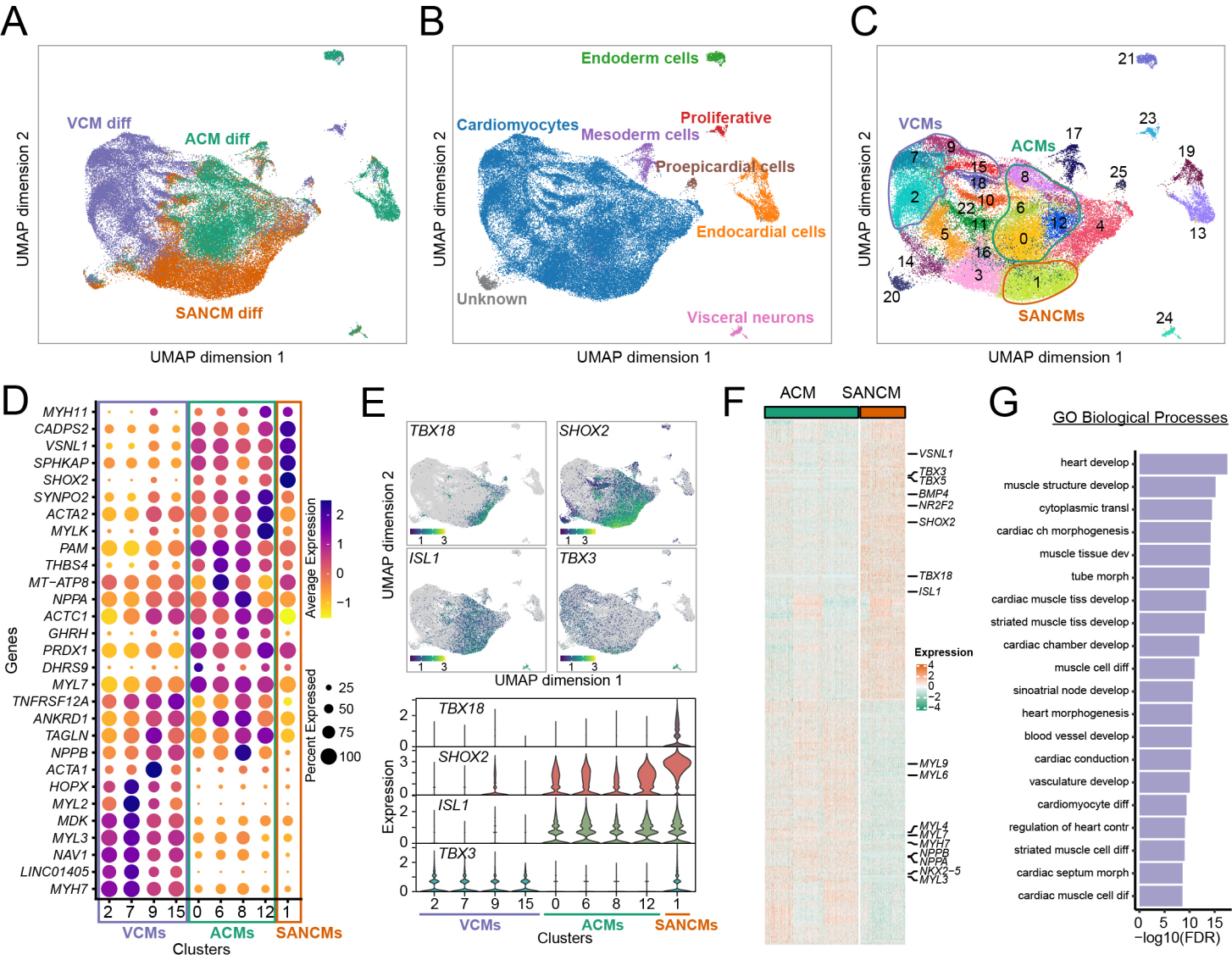
A
VCM diff
ACM diff
SANCM diff
UMAP dimension 2
UMAP dimension 1
B
Endoderm cells
Cardiomyocytes
Mesoderm cells
Proliferative
Proepicardial cells
Endocardial cells
Unknown
Visceral neurons
UMAP dimension 2
UMAP dimension 1
C
VCMs
ACMs
SANCMs
UMAP dimension 2
UMAP dimension 1
D
MYH11
CADPS2
VSNL1
SPHKAP
SHOX2
SYNPO2
ACTA2
MYLK
PAM
THBS4
MT−ATP8
NPPA
ACTC1
GHRH
PRDX1
DHRS9
MYL7
TNFRSF12A
ANKRD1
TAGLN
NPPB
ACTA1
HOPX
MYL2
MDK
MYL3
NAV1
LINC01405
MYH7
Genes
Average Expression
Percent Expressed
VCMs
ACMs
SANCMs
Clusters
E
TBX18
SHOX2
ISL1
TBX3
UMAP dimension 2
UMAP dimension 1
Expression
Clusters
F
ACM
SANCM
VSNL1
TBX3
TBX5
BMP4
NR2F2
SHOX2
TBX18
ISL1
MYL9
MYL6
MYL4
MYL7
MYH7
NPPB
NPPA
NKX2−5
MYL3
Expression
G
GO Biological Processes
heart develop
muscle structure develop
cytoplasmic transl
cardiac ch morphogenesis
muscle tissue dev
tube morph
cardiac muscle tiss develop
striated muscle tiss develop
cardiac chamber develop
muscle cell diff
sinoatrial node develop
heart morphogenesis
blood vessel develop
cardiac conduction
vasculature develop
cardiomyocyte diff
regulation of heart contr
striated muscle cell diff
cardiac septum morph
cardiac muscle cell dif
−log10(FDR)

Figure 3: Sub-cluster analysis of day 34 hiPSC derived SANCMs. (A) Illustration showing the anatomical and functional organization of the Sinoatrial Node (SAN). svc; superior vena cava, cs; coronary sinus, ivc; inferior vena cava, ra; right atrium. (B) Diagram depicting the gradient expression of key transcription factors in the patterning of the Venous Pole. (C) UMAP visualization (top), violin plots showing canonical SANCM marker gene expression in the SANCM clusters (bottom left), and annotation of cell types present (bottom right) in the SANCM differentiation. (D) Dot plot of top 5 marker genes for each cluster in (C). (E) Heatmap of differentially expressed genes between SAN Head cells (cluster 2) and SAN Tail cells (clusters 0 and 3). (F) UMAP of sub-clustered SAN Head cells (cluster 2) and SAN Tail cells (clusters 0 and 3) only. (G) Canonical marker gene expression of sub-clustered SAN Head and SAN Tail cells from (F). (H) Venn diagram showing the overlap of conserved differentially expressed genes (DEGs) from Human iPSC derived SAN Head vs Tail cells (our data) and Mouse *in vivo* isolated SAN Head vs Tail cells (Goodyear et al.).

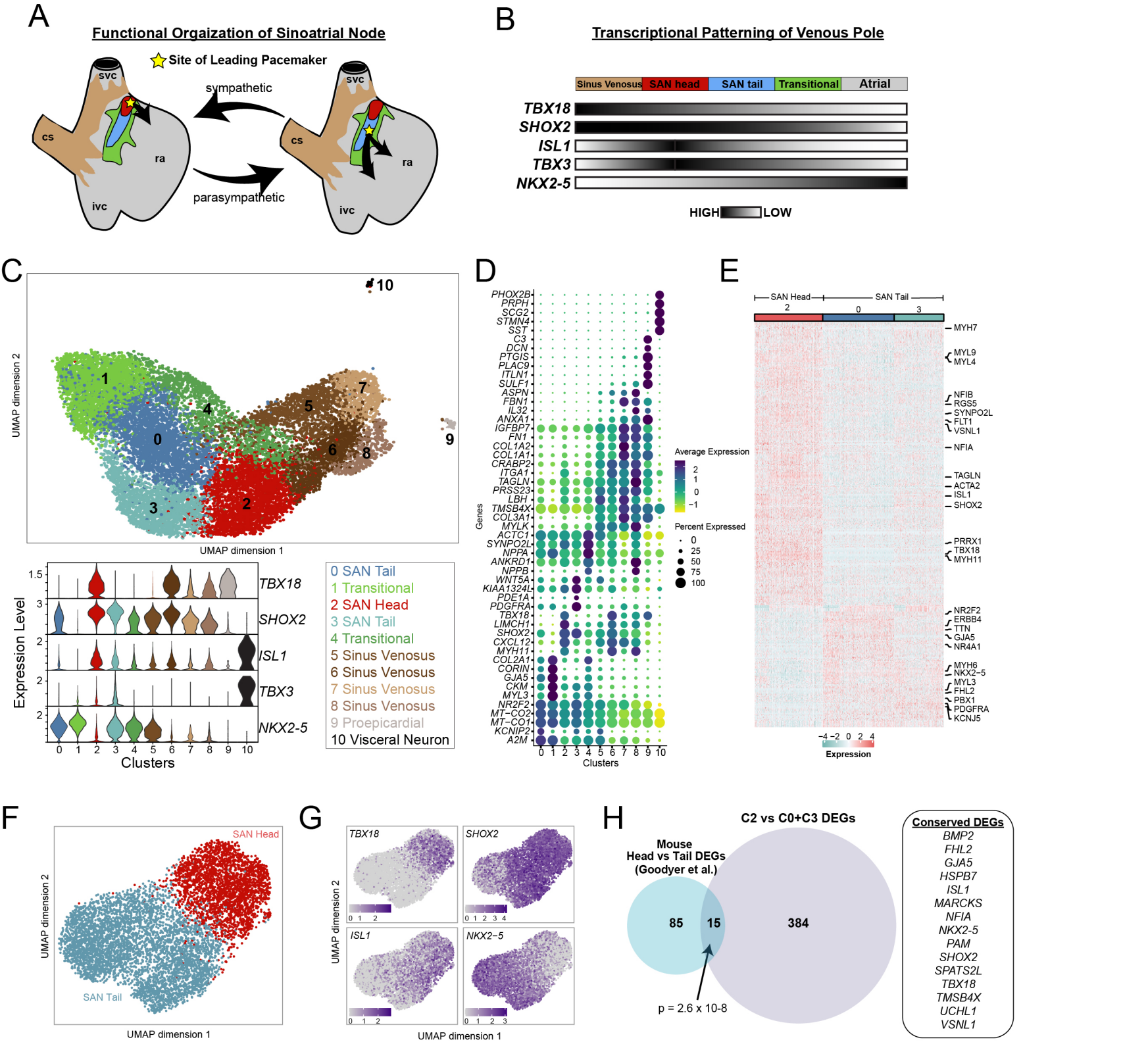
A
Functional Orgaization of Sinoatrial Node
Site of Leading Pacemaker
sympathetic
parasympathetic
svc
cs
ra
ivc
B
Transcriptional Patterning of Venous Pole
Sinus Venosus
SAN head
SAN tail
Transitional
Atrial
TBX18
SHOX2
ISL1
TBX3
NKX2-5
HIGH
LOW
C
UMAP dimension 1
UMAP dimension 2
Expression Level
Clusters
TBX18
SHOX2
ISL1
TBX3
NKX2-5
0 SAN Tail
1 Transitional
2 SAN Head
3 SAN Tail
4 Transitional
5 Sinus Venosus
6 Sinus Venosus
7 Sinus Venosus
8 Sinus Venosus
9 Proepicardial
10 Visceral Neuron
D
Genes
Clusters
Average Expression
Percent Expressed
E
SAN Head
SAN Tail
Expression
F
SAN Head
SAN Tail
UMAP dimension 1
UMAP dimension 2
G
TBX18
SHOX2
ISL1
NKX2-5
UMAP dimension 1
UMAP dimension 2
H
C2 vs C0+C3 DEGs
Mouse
Head vs Tail DEGs
(Goodyer et al.)
85
15
384
p = 2.6 x 10-8
Conserved DEGs
BMP2
FHL2
GJA5
HSPB7
ISL1
MARCKS
NFIA
NKX2-5
PAM
SHOX2
SPATS2L
TBX18
TMSB4X
UCHL1
VSNL1

Figure 4: scATAC-seq analysis of day 34 hiPSC derived SANCMs. (A) UMAP projection and cluster annotation of cell types present. (B) Predicted expression of canonical SANCM marker genes in each cluster from scATAC-seq data. (C) Chromatin accessibility and predicated Peak2gene expression of peaks from scATACseq (left) vs gene expression from scRNA-seq (right) of SANCMs. Accessibility or expression counts are scaled by peak or gene, respectively. (D-F) Genomic tracks for accessibility and predicated Peak2gene links around (D) ISL1, (E) SHOX2 and (F) TBX3 loci for all cell types annotated in (A) recapitulate known key regulatory elements in the SAN. (G) Hypergeometric enrichment of top 20 TF binding motifs in marker peaks of each cluster. (H) Top 10 upregulated and downregulated transcription factor binding motifs in SAN Head cells (cluster 2) versus SAN Tail cells (clusters 1,4 and 6). (I) Top 25 predicated positive regulatory transcription factors whose gene expression is positively correlated to changes in the accessibility of their corresponding motif.

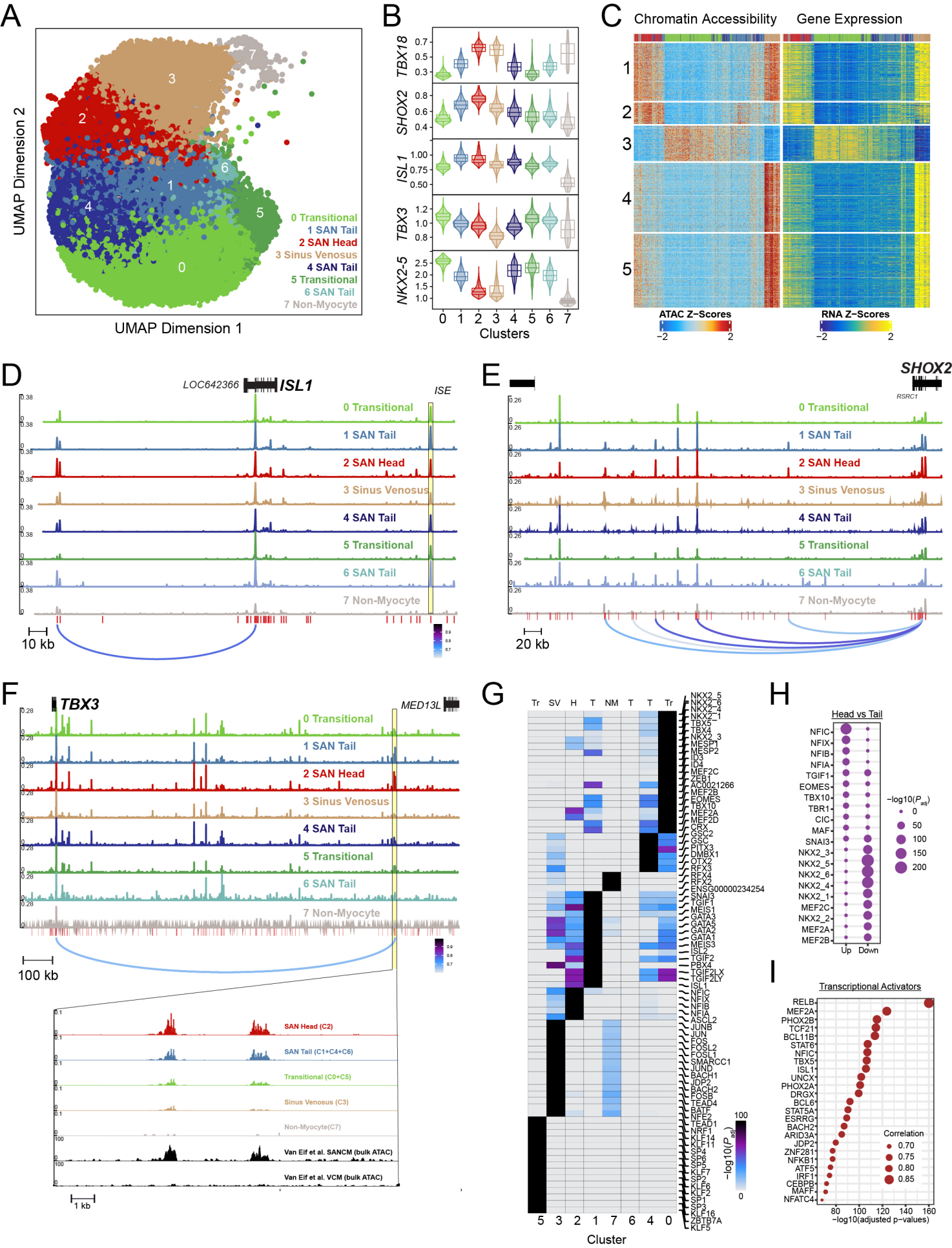
A
UMAP Dimension 2
UMAP Dimension 1
0 Transitional
1 SAN Tail
2 SAN Head
3 Sinus Venosus
4 SAN Tail
5 Transitional
6 SAN Tail
7 Non-Myocyte
B
TBX18
SHOX2
ISL1
TBX3
NKX2-5
Clusters
C
Chromatin Accessibility
Gene Expression
ATAC Z-Scores
RNA Z-Scores
D
LOC642366
ISL1
ISE
10 kb
E
SHOX2
RSRC1
20 kb
F
TBX3
MED13L
100 kb
SAN Head (C2)
SAN Tail (C1+C4+C6)
Transitional (C0+C5)
Sinus Venosus (C3)
Non-Myocyte(C7)
Van Eif et al. SANCM (bulk ATAC)
Van Eif et al. VCM (bulk ATAC)
1 kb
G
Cluster
H
Head vs Tail
Up
Down
I
Transcriptional Activators
Correlation
-log10(adjusted p-values)

Figure 5: Time course scRNA-seq analysis of hiPSC derived SANCMs. (A) UMAP plot of unsupervised clustering with annotated cell types. (B) Schematic of predicted differentiation lineages inferred from PAGA analysis. (C) Diffusion map of clusters in the SAN cell lineage from Day 3, 6, 10, 23, and 34 of differentiation with cells colored by clusters (left) and pseudotime (right). (D) Diffusion map of clusters in the SAN cell lineage from later stages of differentiation (day 23 and 34) with cells colored by clusters (top) and pseudotime (bottom), (E) UMAPs showing canonical SAN marker genes after sub-clustering of TBX18+ progenitors (cluster 14 of fig 5A) from day 6 of differentiation. (F) UMAPs showing canonical SAN marker genes after sub-clustering of Pacemaker progenitors (cluster 5 of fig 5A) from day 10 of differentiation. (G) Dot plot of top 25 upregulated and downregulated DEGs in Early CMs (cluster 5) vs TBX18+ Progenitors (cluster 14). (H) Heatmaps of DEGs from SAN Progenitors (cluster 28) vs SAN Head (clusters 2 of fig 3C; left), SAN Tail (cluster 0 and 3 of fig 3C, center), and SAN Transitional (clusters 1 and 4 of fig 3C, right), respectively.

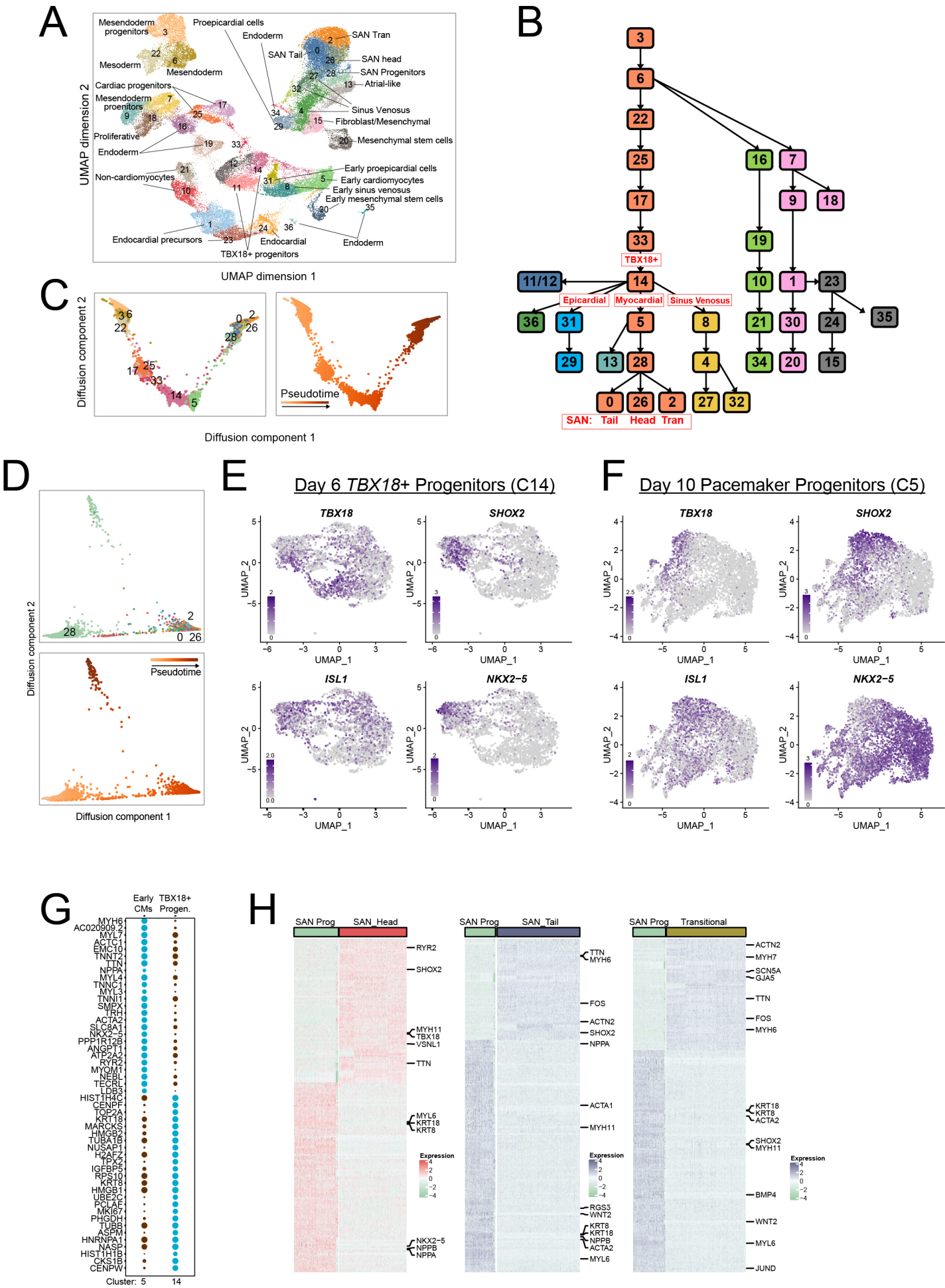
A
Mesendoderm progenitors
Proepicardial cells
Endoderm
SAN Tran
SAN Tail
SAN head
SAN Progenitors
Atrial-like
Mesoderm
Mesendoderm
Cardiac progenitors
Mesendoderm proenitors
Sinus Venosus
Fibroblast/Mesenchymal
Proliferative
Mesenchymal stem cells
Endoderm
Early proepicardial cells
Non-cardiomyocytes
Early cardiomyocytes
Early sinus venosus
Early mesenchymal stem cells
Endocardial precursors
Endocardial
Endoderm
TBX18+ progenitors
UMAP dimension 2
UMAP dimension 1
B
TBX18+
Epicardial
Myocardial
Sinus Venosus
SAN: Tail Head Tran
C
Diffusion component 2
Pseudotime
Diffusion component 1
D
Diffusion component 2
Pseudotime
Diffusion component 1
E
Day 6 TBX18+ Progenitors (C14)
TBX18
SHOX2
ISL1
NKX2−5
UMAP_1
UMAP_2
F
Day 10 Pacemaker Progenitors (C5)
TBX18
SHOX2
ISL1
NKX2−5
UMAP_1
UMAP_2
G
Early CMs
TBX18+ Progen.
MYH6
AC020909.2
MYL7
ACTC1
EMC10
TNNT2
TTN
NPPA
MYL4
TNNC1
MYL3
TNNI1
SMPX
TRH
ACTA2
SLC8A1
NKX2−5
PPP1R12B
ANGPT1
ATP2A2
RYR2
MYOM1
NEBL
TECRL
LDB3
HIST1H4C
CENPF
TOP2A
KRT18
MARCKS
HMGB2
TUBA1B
NUSAP1
H2AFZ
TPX2
IGFBP5
RPS10
KRT8
HMGB1
UBE2C
PCLAF
MKI67
PHGDH
TUBB
ASPM
HNRNPA1
NASP
HIST1H1B
CKS1B
CENPW
Cluster: 5 14
H
SAN Prog
SAN_Head
SAN_Tail
Transitional
RYR2
SHOX2
MYH11
TBX18
VSNL1
TTN
MYL6
KRT18
KRT8
NKX2−5
NPPB
NPPA
TTN
MYH6
FOS
ACTN2
SHOX2
NPPA
ACTA1
MYH11
RGS5
WNT2
KRT8
KRT18
NPPB
ACTA2
MYL6
ACTN2
MYH7
SCN5A
GJA5
TTN
FOS
MYH6
KRT18
KRT8
ACTA2
SHOX2
MYH11
BMP4
WNT2
MYL6
JUND
Expression

Figure 6: Integrative analysis of scATAC-seq data and GWAS. (A) Dot plot showing association of SAN cell types with complex traits and diseases. Cell-type-stratified linkage disequilibrium score regression (LDSC) analysis was performed using GWAS summary statistics for 41 phenotypes. All ATAC peaks identified from each fetal and adult cell type by human enhancer atlas (http://catlas.org/humanenhancer) were used as background for analysis. P-values were corrected using the Benjamini-Hochberg procedure for multiple tests. FDRs of LDSC coefficient are displayed. (B-C) Manhattan plots showing association of SNPs within or ±0.5 kb away from ATAC-seq marker peaks in (B) SAN Head and (C) SAN Tail with Atrial Fibrillation ascertained from the UK Biobank cohort. Red line indicates significance threshold of Bonferroni adjusted P value of 0.05 after pruning the SNPs with LD ($R^2 > 0.1$). Red text indicates novel gene associated SNPs identified in our analyses. (D) Table summarizing the prioritization of novel gene SNPs associated with Atrial Fibrillation identified in SAN Head, SAN Tail and SAN Transitional marker peaks using adjusted p-values from our study. Bold text indicates genes having significant Peak2gene associations.

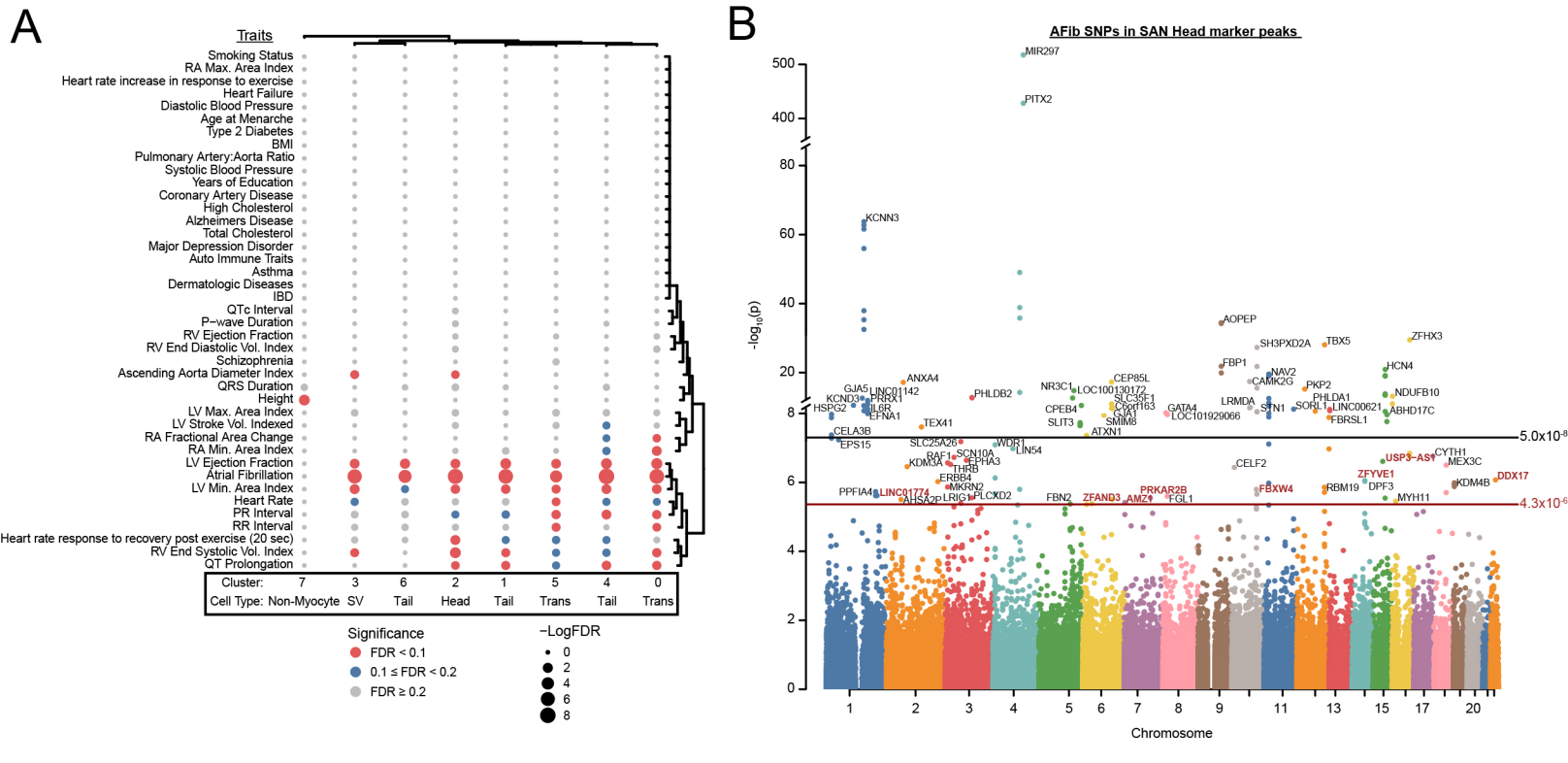

Cell-type:	SAN Head	SAN Tail	SAN Transitional
scATAC-seq cluster(s):	2	1,4,6	0
p-value cutoff:	4.3×10^{-6}	5.6×10^{-6}	3.7×10^{-6}
Genes:	**AMZ1** DDX17 **FBXW4** LINC01774 PRKAR2B USP3-AS1 **ZFAND3** **ZFYVE1**	**ABLIM1** ALDH8A1 DTNA **FBXL20** LINC01774 LOC100506403 **LRCH1** **PARP11** PEX2	**ANKRD44** **GNA12** LOC100506403 LOC101927078 PHTF2 SAMD4A **TBX20** **ZFYVE1**

Extended Data Figure 1: Characterization of hiPSC derived Cardiomyocyte-like subtypes. (A) Beat period as measured by MEA in VCMs, ACMs and SANCMs. (B-D) qPCR for extended (B) pan-cardiac, (C) ventricular and (D) atrial genes in hiPSC derived Cardiomyocyte subtypes. (E) Immunocytochemistry of HCN4 (green) and TNNT2 (red) expression in hiPSC derived VCMs and SANCMs counterstained with Hoescht (blue) and quantification of signal intensities in two replicates. Dotted lines indicate threshold cutoffs for quantification. (F) Table quantifying percent of VCMs and SANCMs expressing TNNT2, HCN4, ISL1, SHOX2 and NKX2-5 from two replicates of immunocytochemistry experiments. (G) ADP20 and ADP90 measurements recorded from VCMs and SANCMs using FluoVolt. Significance was determined using one-way ANOVA with multiple comparisons tests. * $p<0.05$ ** $p<0.01$ *** $p<0.001$ **** $p<0.0001$

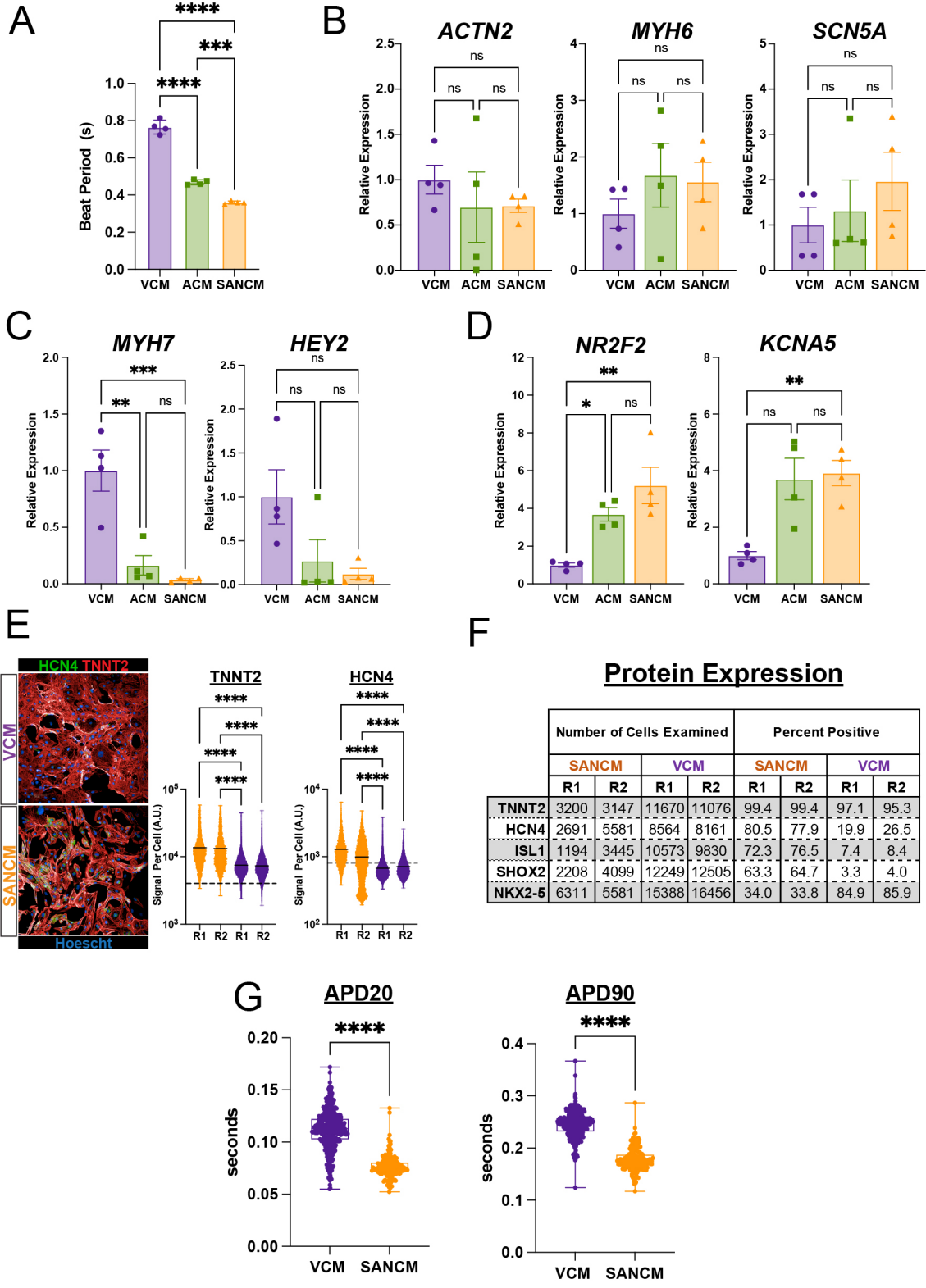

Protein Expression

	Number of Cells Examined				Percent Positive			
	SANCM		VCM		SANCM		VCM	
	R1	R2	R1	R2	R1	R2	R1	R2
TNNT2	3200	3147	11670	11076	99.4	99.4	97.1	95.3
HCN4	2691	5581	8564	8161	80.5	77.9	19.9	26.5
ISL1	1194	3445	10573	9830	72.3	76.5	7.4	8.4
SHOX2	2208	4099	12249	12505	63.3	64.7	3.3	4.0
NKX2-5	6311	5581	15388	16456	34.0	33.8	84.9	85.9

Extended Data Figure 2: scRNA-seq of day 34 hiPSC derived VCMs, ACMs and SANCMs. (A) Summary of scRNA-seq data metrics. (B) Cluster assignments of Fig. 2c based on cell type composition of each cluster. (C) Feature plots showing expression of selected canonical genes used to annotate VCMs and ACMs in Fig. 2c. (D-H) Violin plots showing expression of canonical (D) pan-myocardial, (E) proepicardial, (F) endocardial, (G) primitive mesendoderm, and (H) visceral neuron markers in all clusters in Fig. 2c. (I) Venn diagram showing the comparison of differentially expressed genes in SANCMs vs ACMs with DEGs identified in previously published neonatal mouse and human fetal SAN vs Right atrium datasets.

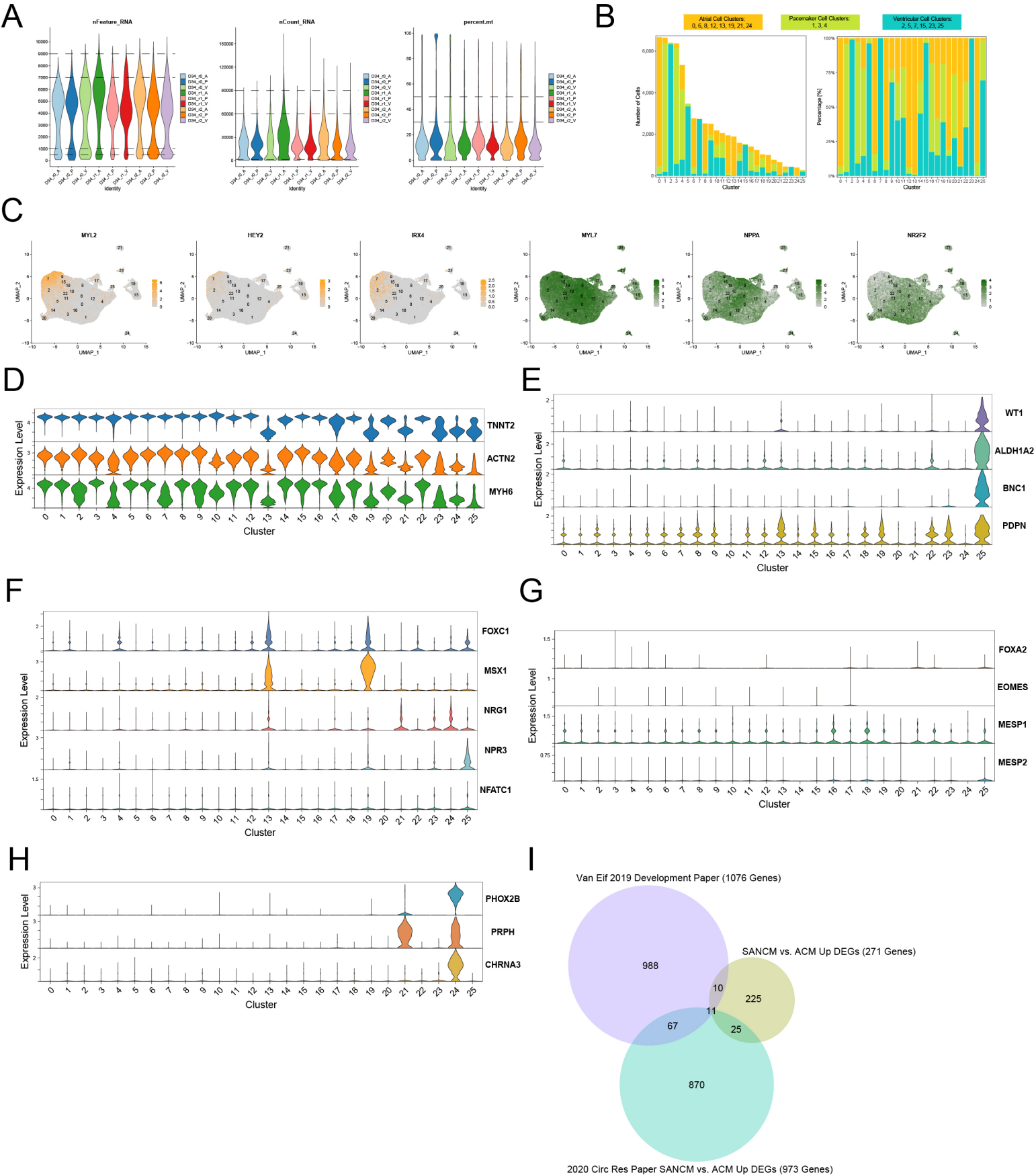
A
nFeature_RNA
nCount_RNA
percent.mt
Identity
B
Atrial Cell Clusters: 0, 6, 8, 12, 13, 19, 21, 24
Pacemaker Cell Clusters: 1, 3, 4
Ventricular Cell Clusters: 2, 5, 7, 15, 23, 25
Number of Cells
Percentage [%]
Cluster
C
MYL2
HEY2
IRX4
MYL7
NPPA
NR2F2
UMAP_1
UMAP_2
D
Expression Level
TNNT2
ACTN2
MYH6
Cluster
E
WT1
ALDH1A2
BNC1
PDPN
F
FOXC1
MSX1
NRG1
NPR3
NFATC1
G
FOXA2
EOMES
MESP1
MESP2
H
PHOX2B
PRPH
CHRNA3
I
Van Eif 2019 Development Paper (1076 Genes)
SANCM vs. ACM Up DEGs (271 Genes)
2020 Circ Res Paper SANCM vs. ACM Up DEGs (973 Genes)
988
10
225
11
67
25
870

Extended Data Figure 3: Sub-cluster comparison of hiPSC derived SANCMs. (A) Mapping of cells from scRNA-seq data from Wiesinger et al. [ref 11] into UMAP scRNA-seq cluster data generated in our study.

A

scRNA-seq clustering from Fig. 3c

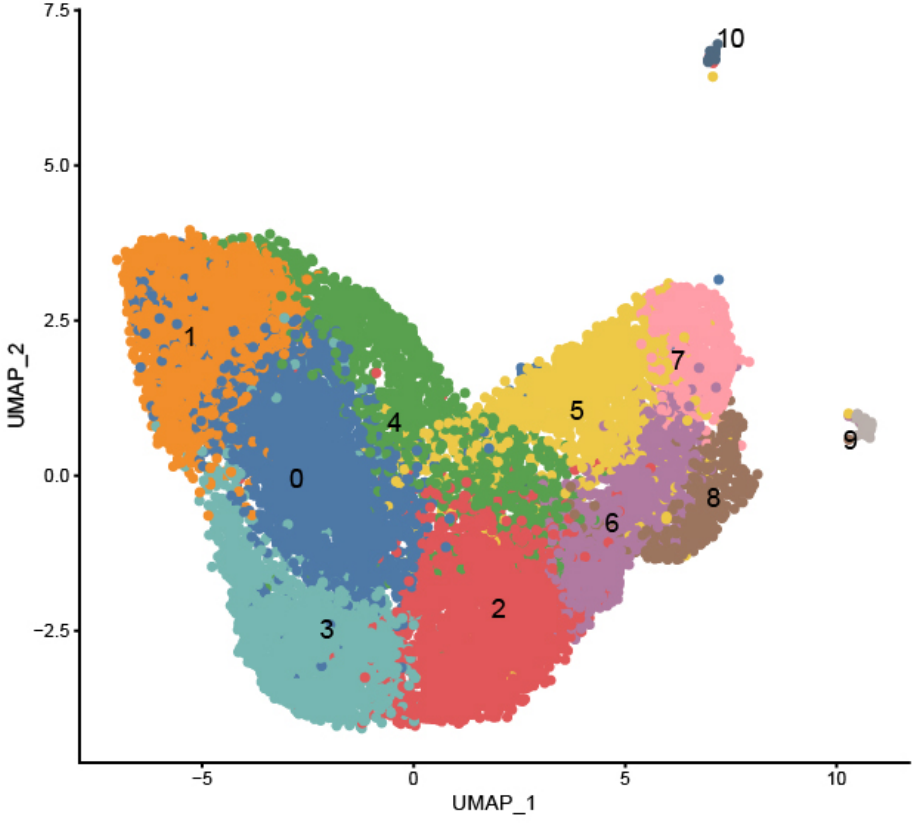

Mapping of Wiesinger et al.
scRNA-seq data onto UMAP from Fig. 3c

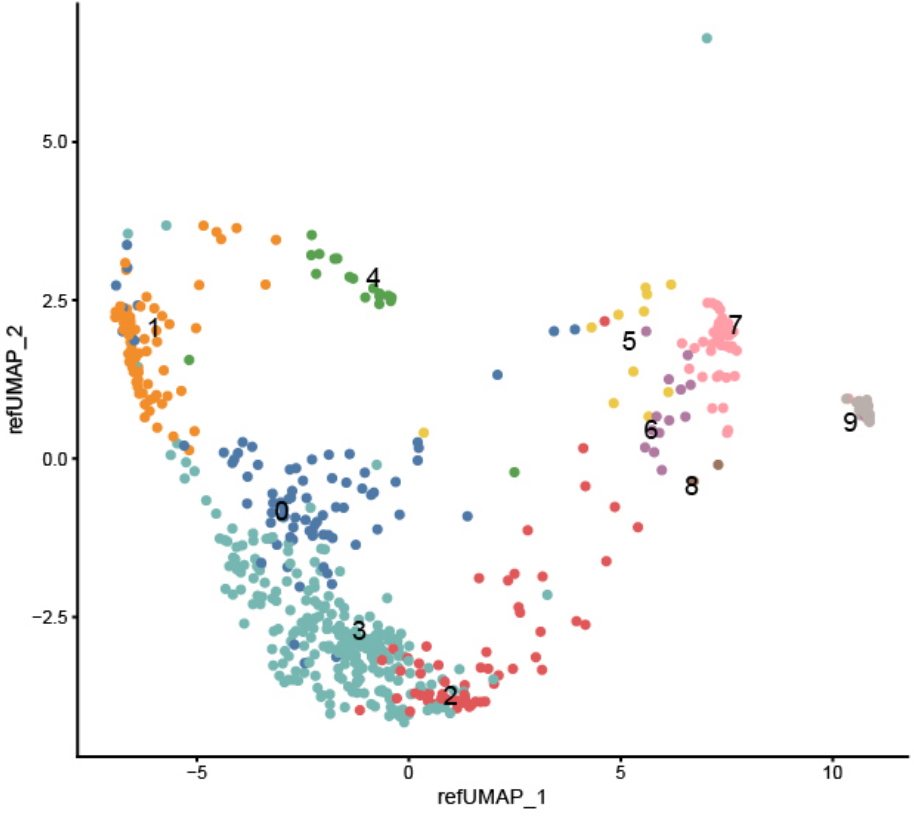

Extended Data Figure 4: scATAC-seq analysis of day 34 hiPSC derived SANCMs. (A) Summary of scATAC-seq data metrics. (B) Genomic tracks for accessibility and predicated Peak2gene links around the TBX18 locus for all cell types annotated in Fig. 4a. (C) Heatmap of predicted gene expression from all clusters in Fig. 4a. (D) Feature plots showing expression of SANCM canonical genes in sub-clustering analysis of SAN Head and SAN Tail only clusters from Fig. 4a.

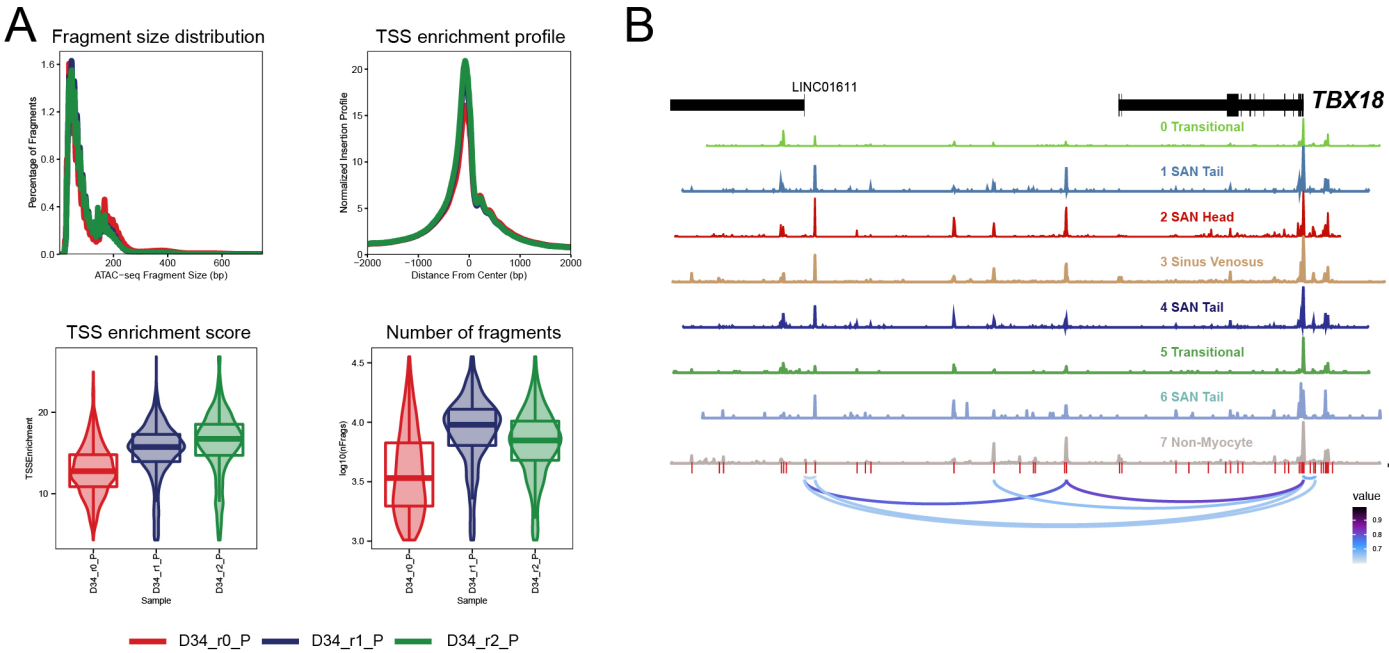
A
Fragment size distribution
Percentage of Fragments
ATAC−seq Fragment Size (bp)
TSS enrichment profile
Normalized Insertion Profile
Distance From Center (bp)
TSS enrichment score
TSSEnrichment
Number of fragments
log10(nFrags)
D34_r0_P
D34_r1_P
D34_r2_P
Sample
B
LINC01611
TBX18
0 Transitional
1 SAN Tail
2 SAN Head
3 Sinus Venosus
4 SAN Tail
5 Transitional
6 SAN Tail
7 Non-Myocyte
value

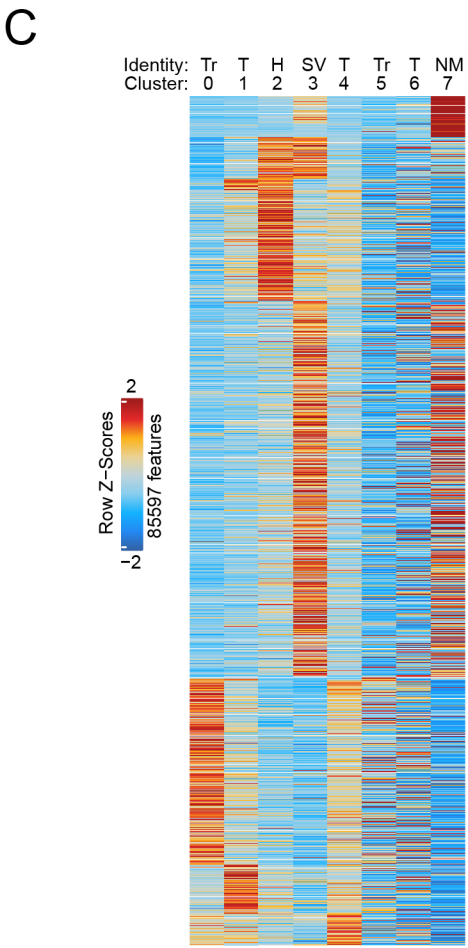
C
Identity: Tr T H SV T Tr T NM
Cluster: 0 1 2 3 4 5 6 7
Row Z−Scores
2
−2
85597 features

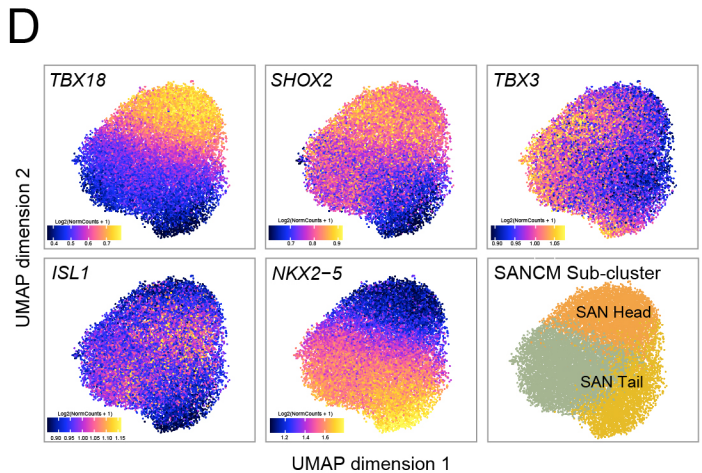
D
TBX18
SHOX2
TBX3
ISL1
NKX2−5
SANCM Sub-cluster
SAN Head
SAN Tail
UMAP dimension 2
UMAP dimension 1

Extended Data Figure 5: Time course scRNA-seq analysis of hiPSC derived SANCMs. (A) Summary of time course scATAC-seq data metrics. (B) Similarity-based connectivity map generated by PAGA analysis. Each cluster is represented as a node and the weighted edges between nodes represent their connectivity. (C) Dot plot of top 25 upregulated and downregulated DEGs in Early Sinus Venosus (SV) (cluster 8) vs TBX18+ Progenitors (cluster 14) (left) and dot plot of top 25 upregulated and downregulated DEGs in Early Proepicardial (PE) (cluster 31) vs TBX18+ Progenitors (cluster 14) (right).

A

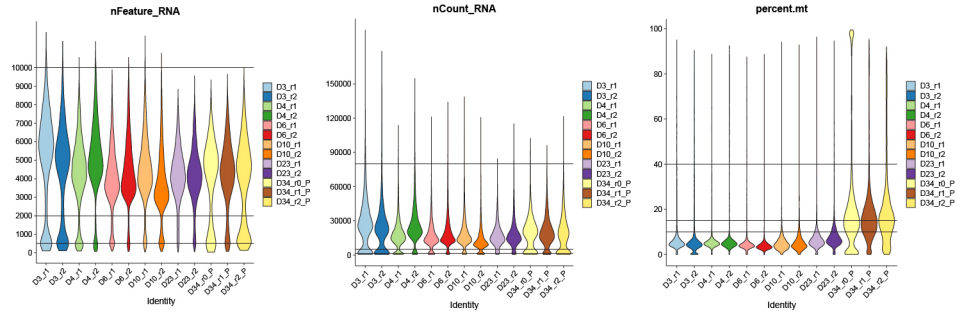
nFeature_RNA
nCount_RNA
percent.mt
Identity
D3_r1
D3_r2
D4_r1
D4_r2
D6_r1
D6_r2
D10_r1
D10_r2
D23_r1
D23_r2
D34_r0_P
D34_r1_P
D34_r2_P

B

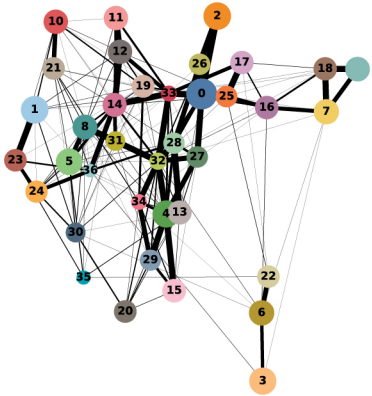

C

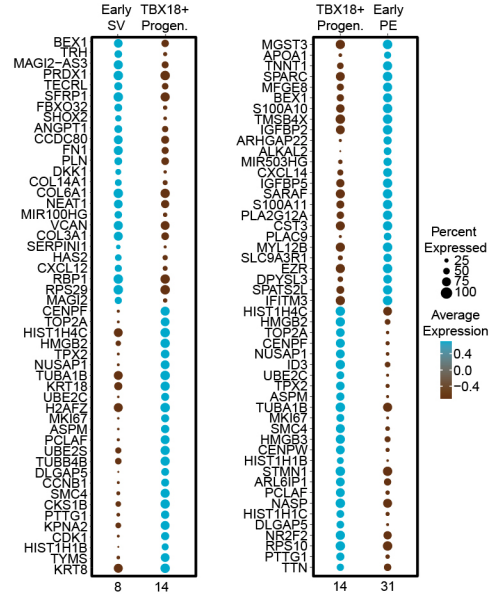
Early SV
TBX18+ Progen.
TBX18+ Progen.
Early PE
BEX1
TRH
MAGI2−AS3
PRDX1
TECR1
SFRP1
FBXO32
SHOX2
ANGPT1
CCDC80
FN1
PLN
DKK1
COL14A1
COL6A1
NEAT1
MIR100HG
VCAN
COL3A1
SERPINI1
HAS2
CXCL12
RBP1
RPS29
MAGI2
CENPF
TOP2A
HIST1H4C
HMGB2
TPX2
NUSAP1
TUBA1B
KRT18
UBE2C
H2AF7
MKI67
ASPM
PCLAF
UBE2S
TUBB4B
DLGAP5
CCNB1
SMC4
CKS1B
PTTG1
KPNA2
CDK1
HIST1H1B
TYMS
KRT8
MGST3
APOA1
TNNT1
SPARC
MFGE8
BEX1
S100A10
TMSB4X
IGFBP3
ARHGAP22
ALKAL2
MIR503HG
CXCL14
IGFBP5
SARAF
S100A11
PLA2G12A
CST3
PLAC9
MYL12B
SLC9A3R1
EZR
DPYSL3
SPATS2L
IFITM3
HIST1H4C
HMGB2
TOP2A
CENPF
NUSAP1
ID3
UBE2C
TPX2
ASPM
TUBA1B
MKI67
SMC4
HMGB3
CENPW
HIST1H1B
STMN1
ARL6IP1
PCLAF
NASP
HIST1H1C
DLGAP5
NR2F2
RPS10
PTTG1
TTN
8
14
14
31
Percent Expressed
25
50
75
100
Average Expression
0.4
0.0
−0.4

Extended Data Figure 6: Integrative analysis of scATAC-seq data and GWAS. (A-B) Manhattan plots showing association of SNPs within or ±0.5 kb away from ATAC-seq marker peaks in (A) all SAN cell types with atrial fibrillation and (B) all SAN cell types with resting heart rate ascertained from the UK Biobank cohort. Red line indicates significance threshold of Bonferroni adjusted P value of 0.05 after pruning the SNPs with LD (R^2 > 0.1). Red text indicates novel gene associated SNPs identified in our analyses. (C-D) Venn diagrams depicting the number of overlapping genome-wide significant genes in (C) atrial fibrillation GWAS studies and (D) heart rate GWAS studies with marker peaks of SANCM clusters in this study.

A

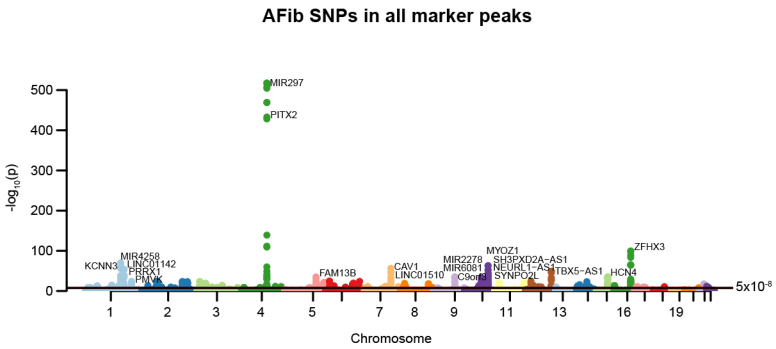
AFib SNPs in all marker peaks
-log10(p)
500
400
300
200
100
0
MIR297
PITX2
KCNN3
MIR4258
LINC01142
PBRX1
PMVK
FAM13B
CAV1
LINC01510
MIR2278
MIR6081
C9orf68
MYOZ1
SH3PXD2A-AS1
NEURL1-AS2
SYNPO2L
TBX5-AS1
HCN4
ZFHX3
5x10-8
1
2
3
4
5
7
8
9
11
13
16
19
Chromosome

B

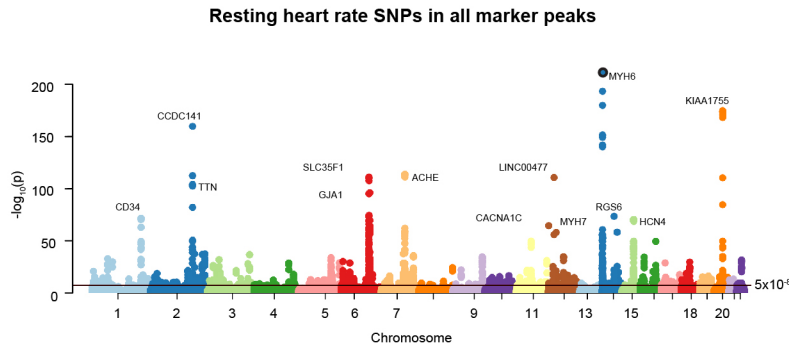
Resting heart rate SNPs in all marker peaks
-log10(p)
200
150
100
50
0
MYH6
KIAA1755
CCDC141
SLC35F1
ACHE
LINC00477
TTN
GJA1
CD34
CACNA1C
MYH7
RGS6
HCN4
5x10-8
1
2
3
4
5
6
7
9
11
13
15
18
20
Chromosome

C

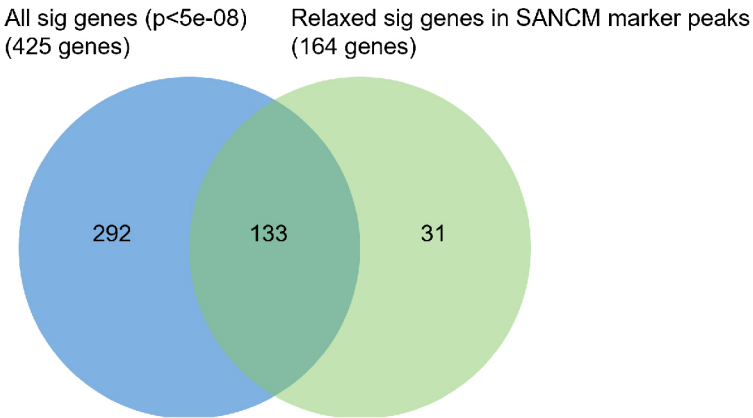
All sig genes (p<5e-08)
(425 genes)
Relaxed sig genes in SANCM marker peaks
(164 genes)
292
133
31

D

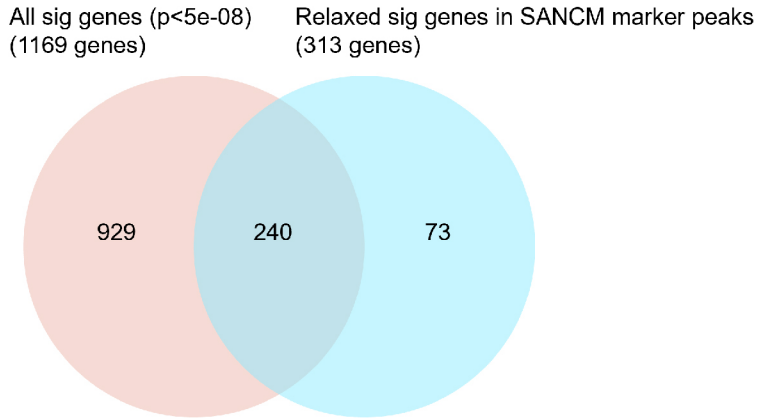
All sig genes (p<5e-08)
(1169 genes)
Relaxed sig genes in SANCM marker peaks
(313 genes)
929
240
73